

CO Multi-line Imaging of Nearby Galaxies (COMING). IX. $^{12}\text{CO}(J=2-1)/^{12}\text{CO}(J=1-0)$ line ratio on kiloparsec scales

Yoshiyuki YAJIMA ^{1,*} Kazuo SORAI ^{1,2,3,4} Yusuke MIYAMOTO ⁵
Kazuyuki MURAOKA ⁶ Nario KUNO ^{3,4,7} Hiroyuki KANEKO ^{8,5}
Tsutomu T. TAKEUCHI ^{9,10} Atsushi YASUDA³ Takahiro TANAKA³
Kana MOROKUMA-MATSUI ¹¹ and Masato I. N. KOBAYASHI ^{12,13}

¹Department of CosmoSciences, Graduate School of Science, Hokkaido University, N10 W8, Kita-ku, Sapporo, Hokkaido 060-0810, Japan

²Department of Physics, Faculty of Science, Hokkaido University, N10 W8, Kita-ku, Sapporo, Hokkaido 060-0810, Japan

³Division of Physics, Graduate School of Pure and Applied Sciences, University of Tsukuba, 1-1-1 Tennodai, Tsukuba, Ibaraki 305-8571, Japan

⁴Tomonaga Center for the History of the Universe, University of Tsukuba, 1-1-1 Tennodai, Tsukuba, Ibaraki 305-8571, Japan

⁵National Astronomical Observatory of Japan, 2-21-1 Osawa, Mitaka, Tokyo 181-8588, Japan

⁶Department of Physical Science, Osaka Prefecture University, 1-1 Gakuen, Sakai, Osaka 599-8531, Japan

⁷Department of Physics, School of Science and Technology, Kwansei Gakuin University, 2-1 Gakuen, Sanda, Hyogo 669-1337, Japan

⁸Graduate School of Education, Joetsu University of Education, 1, Yamayashiki-machi, Joetsu, Niigata 943-8512, Japan

⁹Division of Particle and Astrophysical Science, Nagoya University, Furo-cho, Chikusa-ku, Nagoya, Aichi 464-8602, Japan

¹⁰The Research Center for Statistical Machine Learning, The Institute of Statistical Mathematics, 10-3 Midori-cho, Tachikawa, Tokyo 190-8562, Japan

¹¹Institute of Astronomy, The University of Tokyo, 2-21-1 Osawa, Mitaka, Tokyo 181-0015, Japan

¹²Department of Earth and Space Science, Graduate School of Science, Osaka University, 1-1 Machikaneyama-cho, Toyonaka, Osaka 560-0043, Japan

¹³Astronomical Institute, Graduate School of Science, Tohoku University, Aoba-ku, Sendai, Miyagi 980-8578, Japan

*E-mail: yajima@astro1.sci.hokudai.ac.jp

Received 2020 May 29; Accepted 2020 December 15

Abstract

While molecular gas mass is usually derived from $^{12}\text{CO}(J=1-0)$ —the most fundamental line for exploring molecular gas—it is often derived from $^{12}\text{CO}(J=2-1)$ assuming a constant $^{12}\text{CO}(J=2-1)/^{12}\text{CO}(J=1-0)$ line ratio ($R_{2/1}$). We present variations of $R_{2/1}$ and effects of the assumption that $R_{2/1}$ is a constant in 24 nearby galaxies using ^{12}CO data obtained with the Nobeyama 45 m radio telescope and IRAM 30 m telescope. The median of $R_{2/1}$ for all galaxies is 0.61, and the weighted mean of $R_{2/1}$ by $^{12}\text{CO}(J=1-0)$ integrated intensity is 0.66 with a standard deviation of 0.19. The radial variation of $R_{2/1}$ shows that

it is high (~ 0.8) in the inner ~ 1 kpc while its median in disks is nearly constant at 0.60 when all galaxies are compiled. In the case that the constant $R_{2/1}$ of 0.7 is adopted, we found that the total molecular gas mass derived from $^{12}\text{CO}(J=2-1)$ is underestimated/overestimated by $\sim 20\%$, and at most by 35%. The scatter of molecular gas surface density within each galaxy becomes larger by $\sim 30\%$, and at most by 120%. Indices of the spatially resolved Kennicutt–Schmidt relation by $^{12}\text{CO}(J=2-1)$ are underestimated by 10%–20%, at most 39%, in 17 out of 24 galaxies. $R_{2/1}$ has good positive correlations with star-formation rate and infrared color, and a negative correlation with molecular gas depletion time. There is a clear tendency of increasing $R_{2/1}$ with increasing kinetic temperature (T_{kin}). Further, we found that not only T_{kin} but also pressure of molecular gas is important in understanding variations of $R_{2/1}$. Special considerations should be made when discussing molecular gas mass and molecular gas properties inferred from $^{12}\text{CO}(J=2-1)$ instead of $^{12}\text{CO}(J=1-0)$.

Key words: galaxies: ISM — galaxies: star formation — ISM: molecules — radio lines: galaxies — radio lines: ISM

1 Introduction

Molecular gas is a crucial component in the interstellar medium (ISM) because star formation is the main physical process in the universe, and stars form from cold molecular gas. Therefore, it is essential to understand the properties of molecular gas to investigate galaxies and their evolution. The $^{12}\text{CO}(J=1-0)$ line has been used as a tracer for cold molecular gas (e.g., Solomon et al. 1987; Young & Scoville 1991) because the H_2 molecule cannot be directly observed in cold environments due to having no electric dipole moment. Since the $J=1$ energy level of a ^{12}CO molecule is low ($\Delta E/k_B \sim 5.5$ K, where ΔE is the energy gap and k_B is the Boltzmann constant), ^{12}CO is easily excited to the $J=1$ level and emits the $^{12}\text{CO}(J=1-0)$ line even in cold conditions. In addition, the critical density of $^{12}\text{CO}(J=1-0)$ is a few hundred cubic centimeters in an optically thick region. This value is considerably lower than that of other molecular gas tracers. Furthermore, ^{12}CO is the most abundant molecule in the ISM apart from hydrogen and helium, has large dissociation energy, and its abundance ratio is nearly uniform in molecular clouds. Thus, $^{12}\text{CO}(J=1-0)$ is the most useful line for studying the bulk of cold molecular gas. Molecular gas surface density (Σ_{mol}) in galactic disks is usually derived from the following equation with the integrated intensity of $^{12}\text{CO}(J=1-0)$, $I_{12\text{CO}(1-0)}$,

$$\left(\frac{\Sigma_{\text{mol}}}{M_{\odot} \text{ pc}^{-2}}\right) = 1.36 \times 3.20 \cos i \left(\frac{I_{12\text{CO}(1-0)}}{\text{K km s}^{-1}}\right) \times \left[\frac{X_{\text{CO}}}{2.0 \times 10^{20} \text{ cm}^{-2} (\text{K km s}^{-1})^{-1}}\right], \quad (1)$$

where i is the inclination angle of the galactic disk, and X_{CO} is the CO-to- H_2 conversion factor that converts $I_{12\text{CO}(1-0)}$ into column density of H_2 . The helium in the molecular gas contributes the factor of 1.36, and the other

factor of 3.20 represents the unit conversion of K km s^{-1} into $M_{\odot} \text{ pc}^{-2}$. The product $1.36 \times 3.20 = 4.35$ in units of $M_{\odot} \text{ pc}^{-2} (\text{K km s}^{-1})^{-1}$ corresponding to $X_{\text{CO}} = 2.0 \times 10^{20} \text{ cm}^{-2} (\text{K km s}^{-1})^{-1}$ is also widely used as the CO-to- H_2 conversion factor that converts $I_{12\text{CO}(1-0)}$ into Σ_{mol} [or luminosity of $^{12}\text{CO}(J=1-0)$ into molecular gas mass], usually denoted as “ α_{CO} ” (e.g., Bolatto et al. 2013; Leroy et al. 2013; Schruba et al. 2019).

When the atmosphere is extremely dry, which is common at sites of short-millimeter and submillimeter telescopes, the observation efficiency of $^{12}\text{CO}(J=1-0)$ for the local universe is usually lower than that with $^{12}\text{CO}(J=2-1)$. This is because the rest frequency of $^{12}\text{CO}(J=1-0)$, 115 GHz, is close to the O_2 absorption band at 118 GHz, and the $^{12}\text{CO}(J=2-1)$ attenuation caused by water vapor is small at its rest frequency of 230 GHz in such sites. Thus, $^{12}\text{CO}(J=2-1)$ is often used to observe molecular gas instead of $^{12}\text{CO}(J=1-0)$ (e.g., Leroy et al. 2009, hereafter L09; Druard et al. 2014; Sun et al. 2018). In this case, Σ_{mol} is derived from the following equation instead of equation (1) by assuming the integrated-intensity ratio of $^{12}\text{CO}(J=2-1)/^{12}\text{CO}(J=1-0)$ (hereafter, $R_{2/1}$),

$$\left(\frac{\Sigma_{\text{mol}}}{M_{\odot} \text{ pc}^{-2}}\right) = 1.36 \times 3.20 \cos i R_{2/1}^{-1} \left[\frac{I_{12\text{CO}(2-1)}}{\text{K km s}^{-1}}\right] \times \left[\frac{X_{\text{CO}}}{2.0 \times 10^{20} \text{ cm}^{-2} (\text{K km s}^{-1})^{-1}}\right], \quad (2)$$

where $I_{12\text{CO}(2-1)}$ is the integrated intensity of $^{12}\text{CO}(J=2-1)$. The value of 0.7–0.8 is usually assumed to be a constant $R_{2/1}$ (e.g., L09; Leroy et al. 2013).

Although $^{12}\text{CO}(J=2-1)$ is used as a proxy of $^{12}\text{CO}(J=1-0)$, the energy of the $^{12}\text{CO} J=2$ level ($\Delta E/k_B \sim 16.5$ K) is higher than that in typical cold molecular clouds (~ 10 K). Therefore, it is possible that ^{12}CO molecules are

not sufficiently excited to reach the $J=2$ level based on molecular gas properties (e.g., Peñaloza et al. 2017). Molecular gas traced by $^{12}\text{CO}(J=2-1)$ is warmer and/or denser than that traced using $^{12}\text{CO}(J=1-0)$. $R_{2/1}$ is influenced by the physical conditions of molecular gas.

Systematic variations of $R_{2/1}$ have been reported in previous observations of molecular gas in the Milky Way. For nearby giant molecular clouds (GMCs), while $R_{2/1}$ is medium (~ 0.7 – 0.8) in the ridges of GMCs, it exceeds unity in interfaces of H II regions and OB associations, and it is relatively low in the peripheries of GMCs (~ 0.5 ; Sakamoto et al. 1994; Nishimura et al. 2015). GMCs with active star formation tend to show high $R_{2/1}$, while those with quiescent star formation show low ratios. In large scales of the Milky Way, $R_{2/1}$ decreases from 0.75 at 4 kpc to 0.5 at 8 kpc as a function of the Galactocentric radius (Sakamoto et al. 1995, 1997). Further, an $R_{2/1}$ gradient appears across spiral arms; it gradually increases toward the downstream of the arms. In addition, $R_{2/1}$ shows higher values that are close to unity in the Galactic center compared with the Galactic disk (Oka et al. 1998; Sawada et al. 2001).

For external galaxies, a pioneering study by Braine and Combes (1992) reported that there is a moderate positive correlation between $R_{2/1}$ and infrared (IR) color, and they attempted to infer molecular gas properties from $R_{2/1}$ around the center of nearby galaxies. High $R_{2/1}$ (0.9 with a scatter of ~ 0.3) was reported in the Large Magellanic Cloud (LMC), and positions where $R_{2/1}$ is high do not always coincide with massive star-formation regions (Sorai et al. 2001). It was argued that it reflects dense molecular gas which is ready to form stars, and is not due to gas warmed by radiation from massive stars, whereas the low-metallicity environment in the LMC may also influence $R_{2/1}$. In several nearby galaxies, the median of $R_{2/1}$ in disks is approximately constant (~ 0.8) and $R_{2/1}$ increases (>1) in the center similar to that in the Milky Way (L09), while some galaxies show a nearly constant $R_{2/1}$ over the entire galaxy, including the center (e.g., M 33; Druard et al. 2014). Leroy et al. (2013) reported a median of 0.66 with standard deviations of ~ 0.3 for approximately 30 nearby galaxies. Based on this result, some studies using $^{12}\text{CO}(J=2-1)$ data assumed a constant $R_{2/1} = 0.7$ and converted the intensity of the line into that of $^{12}\text{CO}(J=1-0)$ to derive molecular gas mass and its surface density.

A detailed study to understand $R_{2/1}$ as a probe of molecular gas properties in the extragalactic field reported that while a typical $R_{2/1}$ is ~ 0.7 , it is relatively high (0.8–0.9) in the leading side (the downstream) of the spiral arms and low (0.4–0.6) in the inter-arms for M 51, as well as the Milky Way (Koda et al. 2012). In addition, they found that $R_{2/1}$ increases as surface density of star-formation rate (Σ_{SFR}) and star-formation efficiency (SFE) in this galaxy.

They also suggested that high $R_{2/1}$ is relevant to molecular gas warmed by active star formation and compressed molecular gas before star formation. With regard to $R_{2/1}$ and star formation activity, it was found that the correlation of $R_{2/1}$ with IR color is better than that of $R_{2/1}$ with far-ultraviolet (FUV) and far-IR intensities in M 83 (Koda et al. 2020). It was argued that these are attributed to warm molecular gas heated by dust, UV photons, and cosmic rays from supernovae, considering the high $R_{2/1}$ in the downstream of arms where many massive stars are seen.

As described above, $R_{2/1}$ has systematic variations within and among galaxies, and it reflects molecular gas conditions such as temperature. Hence, it could be possible that molecular gas mass, and its related quantities and relations derived from $^{12}\text{CO}(J=2-1)$ with assumed constant $R_{2/1}$, are misleading (e.g., Momose et al. 2013), although there remains the uncertainty of the CO-to- H_2 conversion factor. It is better to test the validity of the assumption that $R_{2/1}$ is constant, and its effect on derived quantities and relations which are relevant to molecular gas, especially for many types of galaxies. Furthermore, the causes of $R_{2/1}$ variations should be investigated with physical properties of molecular gas.

The largest CO-mapping survey for nearby galaxies in the world, CO Multi-line Imaging of Nearby Galaxies (COMING; Sorai et al. 2019,¹ hereafter S19) was carried out using the FOur-beam REceiver System on the 45 m Telescope (FOREST; Minamidani et al. 2016) installed on the Nobeyama 45 m telescope. COMING mapped 147 nearby galaxies in ^{12}CO , ^{13}CO , and $\text{C}^{18}\text{O } J=1-0$ lines. The addition of other CO-mapping surveys such as Kuno et al. (2007; hereafter K07) and L09 enable us to investigate spatial $R_{2/1}$ variations in many types of nearby galaxies and the effects of the assumption of a constant $R_{2/1}$ over a large galactic area. With those CO data, we verify the assumption of fixed $R_{2/1}$. The key questions in this paper are as follows: (i) How does the assumption of a constant $R_{2/1}$ affect the molecular gas mass and its relevant relations? Is the assumption that $R_{2/1}$ is constant reasonable? (ii) What changes $R_{2/1}$? How does $R_{2/1}$ vary depending on molecular gas properties?

The remainder of the paper is organized as follows. In section 2, the samples of this study, analysis of CO cubes, intensity accuracy of CO considering calibration and pointing, and ancillary data sets are explained. The spatial distribution, statistics, and radial distribution of $R_{2/1}$ are described in the first half of section 3. In the latter half of the section, we report the effects of constant $R_{2/1}$ on molecular gas mass, its scatter within a galaxy, and

¹ See also (<https://astro3.sci.hokudai.ac.jp/radio/coming/>).

the $\Sigma_{\text{SFR}}-\Sigma_{\text{mol}}$ relation (i.e., the molecular gas Kennicutt–Schmidt relation). To investigate the relation of $R_{2/1}$ and molecular gas properties, the correlations of representative quantities and $R_{2/1}$ are examined in the first half of section 4. We attempted to derive the intrinsic properties of molecular gas, number density, and kinetic temperature from $^{12}\text{CO}(J=1-0)$, $^{12}\text{CO}(J=2-1)$, and $^{13}\text{CO}(J=1-0)$ for COMING galaxies and compared them with $R_{2/1}$. These discussions and implications are described in the latter half of section 4. Finally, the conclusions of this paper are provided in section 5.

2 Data sets

2.1 CO data and their analysis

The $^{12}\text{CO}(J=1-0)$ data used in this paper were taken from COMING in the first instance. Refer to sections 3 and 4 in [S19](#) for details about the settings of observations, calibration, and data reduction for COMING. In addition, the Nobeyama CO Atlas of Nearby Spiral Galaxies ([K07](#)) is used as the second reference for $^{12}\text{CO}(J=1-0)$ data. Since the samples of [K07](#) include galaxies which appear large, it makes it possible to discuss variations of $R_{2/1}$ over a large galactic area. For the $^{12}\text{CO}(J=2-1)$ reference we use the HERA CO-Line Extragalactic Survey (HERACLES; [L09](#)) carried out with the IRAM 30 m telescope.

The $^{12}\text{CO}(J=1-0)$ data obtained by [K07](#) and $^{12}\text{CO}(J=2-1)$ data obtained by [L09](#) were convolved to match the angular resolution of $17''$, which is the original resolution of COMING. Before measurements of $R_{2/1}$, the coordinates for all CO cubes were matched and regridded so that the grid size becomes $8''$. Then, velocity channels were binned so that the velocity resolution is 20 km s^{-1} . These processes were performed to improve the signal-to-noise ratio (S/N). After that, the baseline was subtracted.

The method of baseline subtraction is the same as the COMING Auto-Reduction Tool (COMING ART; see subsection 4.2 in [S19](#) for details); however, signal channels are defined by $^{12}\text{CO}(J=2-1)$, not by $^{12}\text{CO}(J=1-0)$ because $^{12}\text{CO}(J=2-1)$ data achieves a much better sensitivity than $^{12}\text{CO}(J=1-0)$. That is, the result of whether the channel is “signal” or “noise” for each channel of $^{12}\text{CO}(J=2-1)$ in a position was applied to $^{12}\text{CO}(J=1-0)$ at the channel of the same velocity in the position. This methodology does not induce any biases for $^{12}\text{CO}(J=1-0)$ and $^{12}\text{CO}(J=2-1)$ integrated intensities because the sensitivities of the $^{12}\text{CO}(J=2-1)$ data are much better than those of $^{12}\text{CO}(J=1-0)$. The threshold to evaluate each channel as “signal” or “noise” is set as 3σ , where σ is the root mean square (rms) measured in the defined emission-free velocity range beforehand.

Table 1. Samples in this study.*

| Galaxy | D [Mpc] (1) | i [°] (2) | P.A. [°] (3) | Res. [kpc] (4) | Reference of $^{12}\text{CO}(1-0)$ (5) |
|----------|---------------------|-------------------|--------------------|----------------------|--|
| NGC 337 | 18.9 | 44.5 | 119.6 | 1.6 | S19 |
| NGC 628 | 9.02 | 7 | 20 | 0.74 | S19 |
| NGC 2146 | 27.7 | 62 | −43.5 | 2.3 | S19 |
| NGC 2798 | 29.6 | 60.7 | 158.7 | 2.4 | S19 |
| NGC 2841 | 14.60 | 73.7 | 152.6 | 1.2 | S19 |
| NGC 2903 | 9.46 | 67 | −155 | 0.78 | S19 |
| NGC 2976 | 3.63 | 64.5 | −25.5 | 0.30 | S19 |
| NGC 3034 | 3.53 | 81 | 68 | 0.34 | S19 |
| NGC 3077 | 3.81 | 38.9 | 63.8 | 0.31 | S19 |
| NGC 3184 | 8.7 | 21 | −174 | 0.72 | K07 |
| NGC 3198 | 13.40 | 71.5 | −145.0 | 1.1 | S19 |
| NGC 3351 | 10.7 | 41 | −168 | 0.88 | K07 |
| NGC 3521 | 14.20 | 63 | −19 | 1.2 | S19 |
| NGC 3627 | 9.04 | 52 | 176 | 0.75 | S19 |
| NGC 3938 | 17.9 | 20.9 | −154.0 | 1.5 | S19 |
| NGC 4214 | 2.93 | 30 | 65 | 0.24 | S19 |
| NGC 4254 | 16.5 | 42 | 66 | 1.4 | K07 |
| NGC 4321 | 16.5 | 27 | 138 | 1.4 | K07 |
| NGC 4536 | 16.5 | 64.2 | −54.5 | 1.4 | S19 |
| NGC 4559 | 7.31 | 63.1 | −36.8 | 0.60 | S19 |
| NGC 4569 | 16.5 | 64 | 22 | 1.4 | K07 |
| NGC 4579 | 16.5 | 41.7 | 92.1 | 1.4 | S19 |
| NGC 4736 | 4.3 | 40 | −61 | 0.4 | K07 |
| NGC 5055 | 9.04 | 61 | 98 | 0.75 | S19 |
| NGC 5194 | 7.7 | 20 | 176 | 0.63 | K07 |
| NGC 5457 | 7.2 | 18 | 42 | 0.59 | K07 |
| NGC 5713 | 19.5 | 33 | −157 | 1.6 | S19 |
| NGC 6946 | 5.5 | 40 | −118 | 0.5 | K07 |
| NGC 7331 | 13.90 | 75.8 | 167.7 | 1.1 | S19 |

* (1) Adopted distance. (2) Inclination angle of the disk. (3) Position angle of the major axis of the disk for the redshifted side (against the north direction, positive values corresponding to the counterclockwise direction). (4) The linear scale corresponding to an angular resolution of $17''$ along the major axis of the disk. (5) References for $^{12}\text{CO}(J=1-0)$ data. References for D , i , P.A. are the same as in [S19](#) or [K07](#).

The samples in this study consist of 29 galaxies that are overlapped between [S19](#) + [K07](#), and [L09](#). They are listed in table 1. For the overlapped galaxies between [S19](#) and [K07](#) (NGC 2903, NGC 3351, NGC 3521, NGC 3627, NGC 5055), we used [S19](#) data except for NGC 3351 because the baseline of the [S19](#) data for this galaxy is heavily undulated.

2.2 Intensity accuracy of CO data regarding calibration and pointing error

Intensity accuracy of CO data is important in studying $R_{2/1}$ because its contrast is relatively small (usually $R_{2/1} = 0.4-1.0$), as argued in Koda et al. (2012, 2020). Therefore, calibration and pointing error is an issue in this paper.

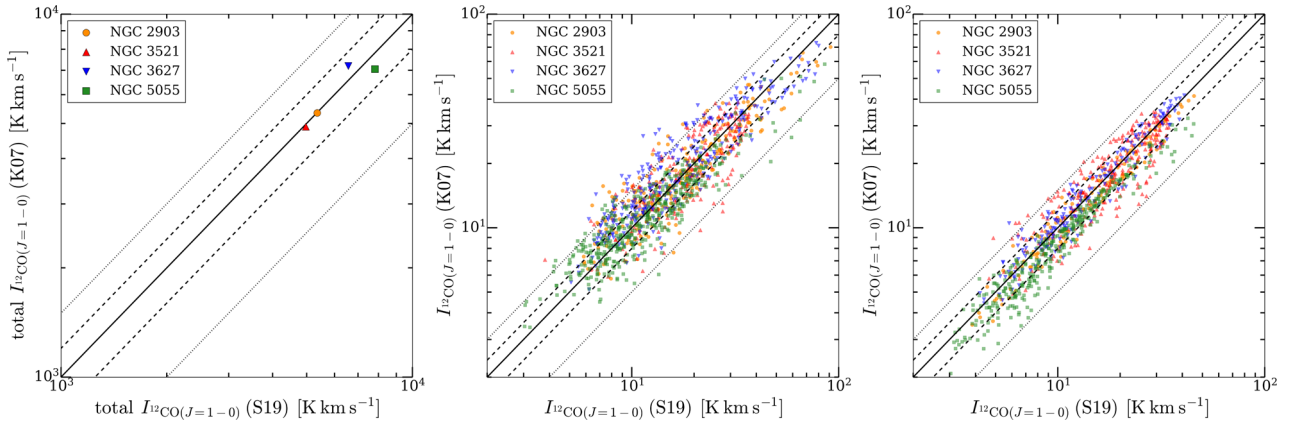


Fig. 1. Consistency of integrated intensity for NGC 2903, NGC 3521, NGC 3627, and NGC 5055 between **S19** and **K07**, summing over the whole disk, which corresponds to the total flux (left), at the original resolution and grid size (center), and convolved data so that the resolution and grid size are fixed to 1.5 kpc and 650 pc (right). Pixels below 5σ are masked in the center and right panels. The solid, dashed, and dotted lines in each panel indicate inconsistency of 0%, $\pm 20\%$, and $\pm 50\%$, respectively. (Color online)

We demonstrated how the intensity of $^{12}\text{CO}(J = 1-0)$ data is accurate with four overlapped galaxies (NGC 2903, NGC 3521, NGC 3627, NGC 5055) between **S19** and **K07**. Although NGC 3351 is an overlapped galaxy, the baseline of this galaxy is heavily undulated and thus we excluded it in testing intensity consistency. Both **S19** and **K07** data was regridded and the baseline was subtracted as described in the previous subsection.

We first tested the consistency of the total integrated intensity within the whole disk (i.e., total flux) for **S19** and **K07** data and the position-to-position integrated intensity in the original resolution ($17''$) and grid size ($8''$). The left and center panels of figure 1 show correlations of total integrated intensities and integrated intensities at each pixel, respectively. The threshold was set to be 5σ in the central panel. The difference in total integrated intensity is at most $\sim 10\%$. The scatter of position-to-position intensity is $\sim 25\%$ in the rms level within each galaxy. Hence, the calibration error of $^{12}\text{CO}(J = 1-0)$ used in this paper is up to 10% and the intensity accuracy, including pointing error and calibration error, is 25% at the original resolution.

In subsections 3.3 and 4.1 we use convolved CO data so that the spatial resolution and grid size are fixed to 1.5 kpc and 650 pc, respectively. In addition, we stacked spectra within concentric annuli in disks and galactic structures in the analyses of subsection 4.2. Thus, we next tested the consistency of convolved **S19** and **K07** data to match a resolution of 1.5 kpc and grid size of 650 pc. The right panel of figure 1 shows the consistency of integrated intensity between **S19** and **K07** for convolved data. The position-to-position scatter in this case is $\sim 15\%$ in each galaxy. Therefore, the intensity error combining calibration and pointing error in subsections 3.3 and 4.1 is 15%. Since, in stacking analysis, spectra are stacked over a large area (galactic

components and concentric annuli whose width is $r_{25}/8$, where r_{25} is the *B*-band isophotal radius at 25 mag arcsec $^{-2}$), the intensity error due to pointing error will be negligible.

We would like to note that the intensity accuracy of $^{13}\text{CO}(J = 1-0)$ against $^{12}\text{CO}(J = 1-0)$ is relatively good because $^{13}\text{CO}(J = 1-0)$ data was taken simultaneously with $^{12}\text{CO}(J = 1-0)$ in COMING observations. In addition, since COMING applied the on-the-fly (OTF) mode in their observation, while observation in **K07** applied position-switch, the calibration and pointing accuracy of **S19** would be better than that of **K07**.

We could not test the calibration/pointing error of $^{12}\text{CO}(J = 2-1)$ data in the same way as **S19** and **K07** because there is no available archival data of the line. However, **L09** mentioned that daily variations of $^{12}\text{CO}(J = 2-1)$ intensity in high-S/N regions were 20%. Therefore, the intensity error of $^{12}\text{CO}(J = 2-1)$ combining calibration and pointing error is 20%, which is considerably better than that of $^{12}\text{CO}(J = 1-0)$. Assuming that the fraction of contribution due to pointing error is the same as the $^{12}\text{CO}(J = 1-0)$ case, the calibration error of $^{12}\text{CO}(J = 2-1)$ will be $\sim 8\%$. Hence, there will also be a calibration error of $\sim 10\%$ in $^{12}\text{CO}(J = 2-1)$ data, which is common in short millimeter-wave observations. Similarly, the intensity error due to calibration/pointing error in convolved $^{12}\text{CO}(J = 2-1)$ data will be $\sim 12\%$. To summarize, the $R_{2/1}$ error due to calibration error is 13%, due to calibration+pointing error at the original angular resolution is 32%, and at fixed spatial resolution and grid size is 19%.

2.3 Data at other wavelengths

Star-formation rate (SFR) was derived from FUV and $22\mu\text{m}$ -band intensity based on the following equation by

Casasola et al. (2017) and Leroy et al. (2008) that adopted the Kroupa initial mass function (IMF; Kroupa 2001) as with the method in other COMING papers (e.g., Muraoka et al. 2019; T. T. Takeuchi et al. in preparation):

$$\left(\frac{\Sigma_{\text{SFR}}}{M_{\odot} \text{ yr}^{-1} \text{ kpc}^{-2}} \right) = 1.59 \cos i \left[3.2 \times 10^{-3} \left(\frac{I_{22\mu\text{m}}}{\text{MJy sr}^{-1}} \right) + 8.1 \times 10^{-2} \left(\frac{I_{\text{FUV}}}{\text{MJy sr}^{-1}} \right) \right], \quad (3)$$

where $I_{22\mu\text{m}}$ and I_{FUV} are the intensities of the $22\mu\text{m}$ and FUV bands. The FUV maps were obtained with the GALEX Ultraviolet Atlas of Nearby Galaxies (Gil de Paz et al. 2007) and were retrieved from the NASA/IPAC Extragalactic Database (NED). The $22\mu\text{m}$ maps obtained with WISE band 4 were retrieved from the NASA/IPAC Infrared Science Archive.

In addition, the IR color that represents dust temperature is used as an indicator of ISM conditions. To measure the IR color in many galaxies as much as possible, we used the intensity ratio of the $70\mu\text{m}$ to $160\mu\text{m}$ band obtained with Herschel/PACS. This filter selection reduces the sample number of galaxies because of a lack of samples in the far-infrared range.

3 Results

3.1 Maps, histograms, statistics, and radial distribution of $R_{2/1}$

Figure 2 shows the $R_{2/1}$ maps for our sample galaxies in the original resolution of COMING ($17''$). Here, the error in $R_{2/1}$ is derived from that of $I_{12\text{CO}(1-0)}$ and $I_{12\text{CO}(2-1)}$ based on propagation of their error. Each galaxy shows various $R_{2/1}$ values. For example, NGC 2798 and NGC 4736 show higher (>0.9) $R_{2/1}$ over a large area. $R_{2/1}$ is low (<0.6) in most positions of NGC 2841 and NGC 3627. Some galaxies have significant variations within each galaxy. NGC 2146 and NGC 5713 show an $R_{2/1}$ gradient from ~ 1.2 to 0.4 . In NGC 4321, $R_{2/1}$ is clearly high ($\gtrsim 1.0$) in the center and bar ends, low ($\lesssim 0.6$) in inter-arm regions, and intermediate (0.7 – 0.8) in the arms. In NGC 3351 and NGC 4579, $R_{2/1}$ is low in the ring-like structure, whereas $R_{2/1}$ is high in the center.

Some galaxies show a gradation of $R_{2/1}$ from one side to the other (e.g., NGC 2146, NGC 2798, NGC 5713, NGC 7331). We tested whether these gradations are due to the systematic pointing offset between $^{12}\text{CO}(J=1-0)$ and $^{12}\text{CO}(J=2-1)$ observations with spectra at some doubtful positions and residual maps of the first moment maps derived from the lines. According to the test, there is no indication of a systematic pointing offset. Gradations

of $R_{2/1}$ may be caused by interactions (e.g., NGC 2146, NGC 2798, NGC 5713) or the appearance of the disk due to three-dimensional warp (NGC 7331).

Note that the result for NGC 5194 is not consistent with Koda et al. (2012). They reported that the intensities of $^{12}\text{CO}(J=1-0)$ data obtained in K07 (the original map is from Nakai et al. 1994) for this galaxy are ~ 2 times higher than Koda et al. (2011). They argued that a calibration error in the data of Nakai et al. (1994) was caused by difficulties in the calibration method at that time.

Figure 3 shows a histogram of $R_{2/1}$ and the cumulative distribution function for all pixels in all galaxies in the samples. As shown in the figure, the constant value of 0.7 assumed in many cases so far is rather large. The peak of the histogram is in the range 0.55 – 0.60 ; the most frequently appearing value of $R_{2/1}$ is lower than 0.7 . The cumulative fraction also indicates that $R_{2/1} = 0.7$ is quite high in our samples (the cumulative fraction at $R_{2/1} = 0.7$ is $\sim 70\%$). This is significant even considering the $R_{2/1}$ error of 13% due to the calibration error of CO data. The median, mean weighted by $^{12}\text{CO}(J=1-0)$ integrated intensity, and standard deviation of $R_{2/1}$ combined for all galaxies are 0.61 , 0.66 , and 0.19 , respectively.

The median we obtained ($R_{2/1} = 0.61$) is slightly lower than the value ($R_{2/1} = 0.67$) reported by Leroy et al. (2013), while this difference may not be significant considering that the $R_{2/1}$ error due to calibration error is 13% (subsection 2.2). If this difference is significant, this discrepancy may have originated from differences in observed areas. Most $^{12}\text{CO}(J=1-0)$ data Leroy et al. (2013) used are from Usero et al. (2015), which observed specific positions in a galaxy where $^{12}\text{CO}(J=2-1)$ is strong. Their observed areas in each galaxy usually include the center of the galaxy where $R_{2/1}$ tends to be high, as mentioned in the next paragraph. These results and statistics of $R_{2/1}$ such as median, $Q_2(R_{2/1})$, and weighted mean, $\overline{R}_{2/1}$, for each galaxy are summarized in table 2 with some properties of galaxies related to star formation. The relations between $R_{2/1}$ and these properties of galaxies are discussed in subsection 4.1. Histograms of $R_{2/1}$ for each galaxy are shown in appendix 1.

Figure 4 shows $R_{2/1}$ as a function of the galactocentric radius for all galaxies. Both the median and weighted mean of $R_{2/1}$ in the disk region ($r > 2 \text{ kpc}$) are nearly constant at 0.60 . Although $R_{2/1}$ in the disk is lower than 0.7 , it tends to exceed 0.7 in central regions. Both the median and weighted mean are 0.83 in the inner 0.75 kpc (the innermost bin of the bottom panel of figure 4). The usually assumed constant value of 0.7 for $R_{2/1}$ is common only for the transition region of the galactic center and the disk ($1 \text{ kpc} \lesssim r \lesssim 2 \text{ kpc}$).

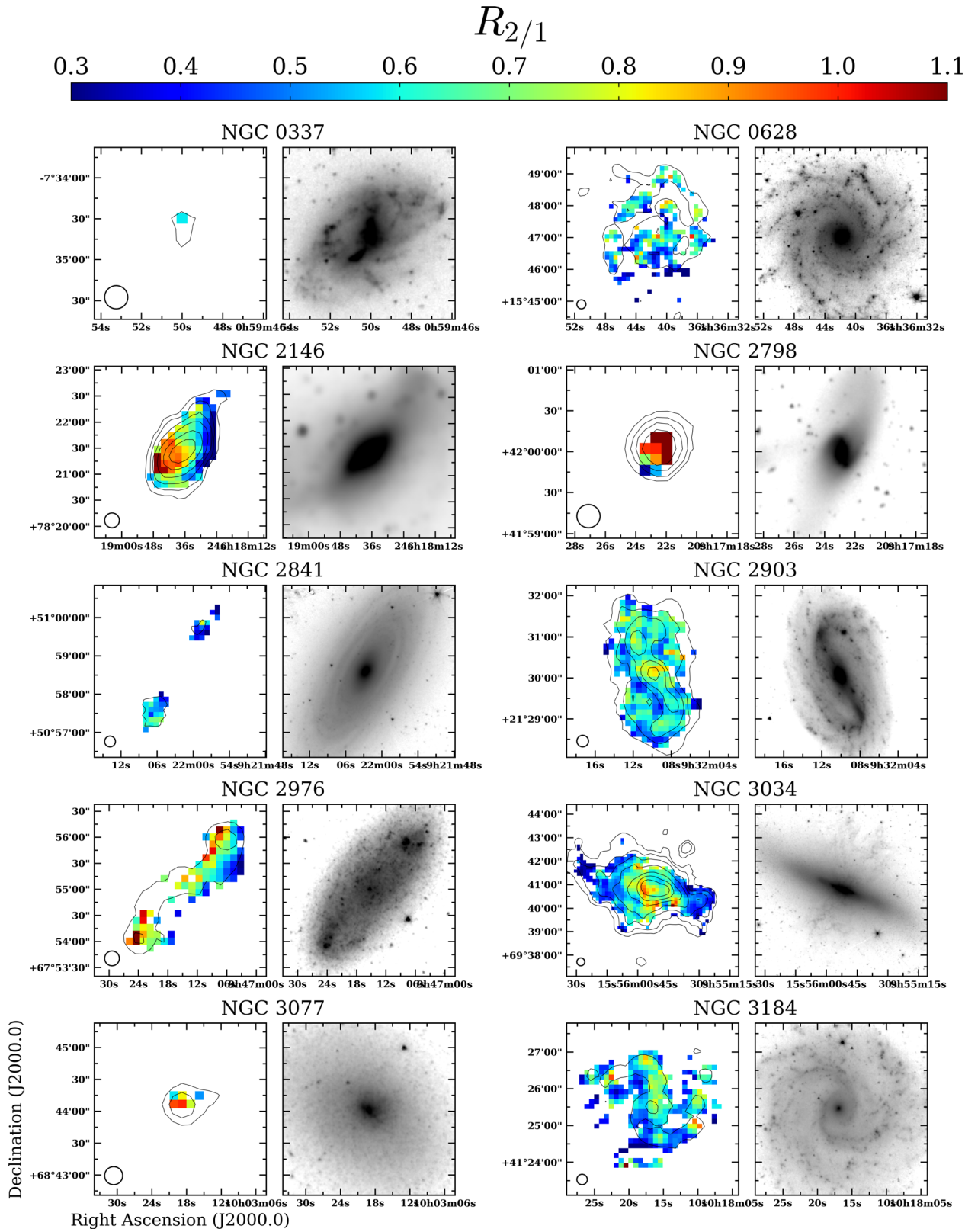


Fig. 2. $R_{2/1}$ maps (left) and near-infrared images in gray scale (right) of all galaxies in the samples. In the $R_{2/1}$ maps, pixels are masked when either integrated intensities of $^{12}\text{CO}(J=1-0)$ or $^{12}\text{CO}(J=2-1)$ at the pixel do not reach 4.5σ . The middle of the color bar corresponds to $R_{2/1} = 0.7$, which is the usually assumed value for a constant $R_{2/1}$. The open circles in the bottom left corner in each panel indicate an angular resolution of $17''$. Black contours indicate the integrated intensity of $^{12}\text{CO}(J=2-1)$ at levels 2, 5, 10, 20, 50, 100, and 200 K km s^{-1} . The reference for near-infrared data is Spitzer/IRAC $3.6\mu\text{m}$ images obtained by the S⁴G survey (Sheth et al. 2010), except for NGC 2146. For NGC 2146, the WISE $3.4\mu\text{m}$ image is used. (Color online)

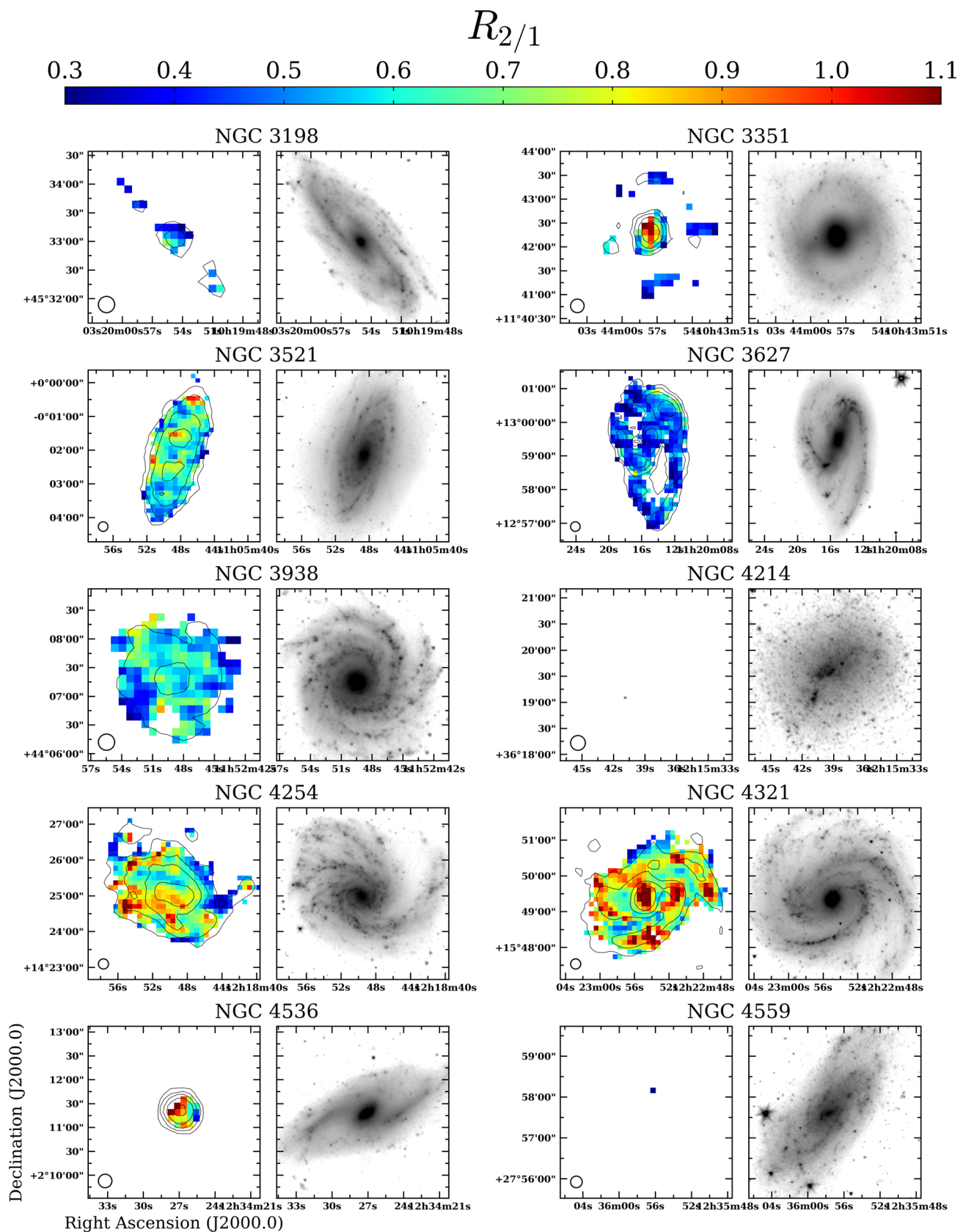


Fig. 2. (Continued)

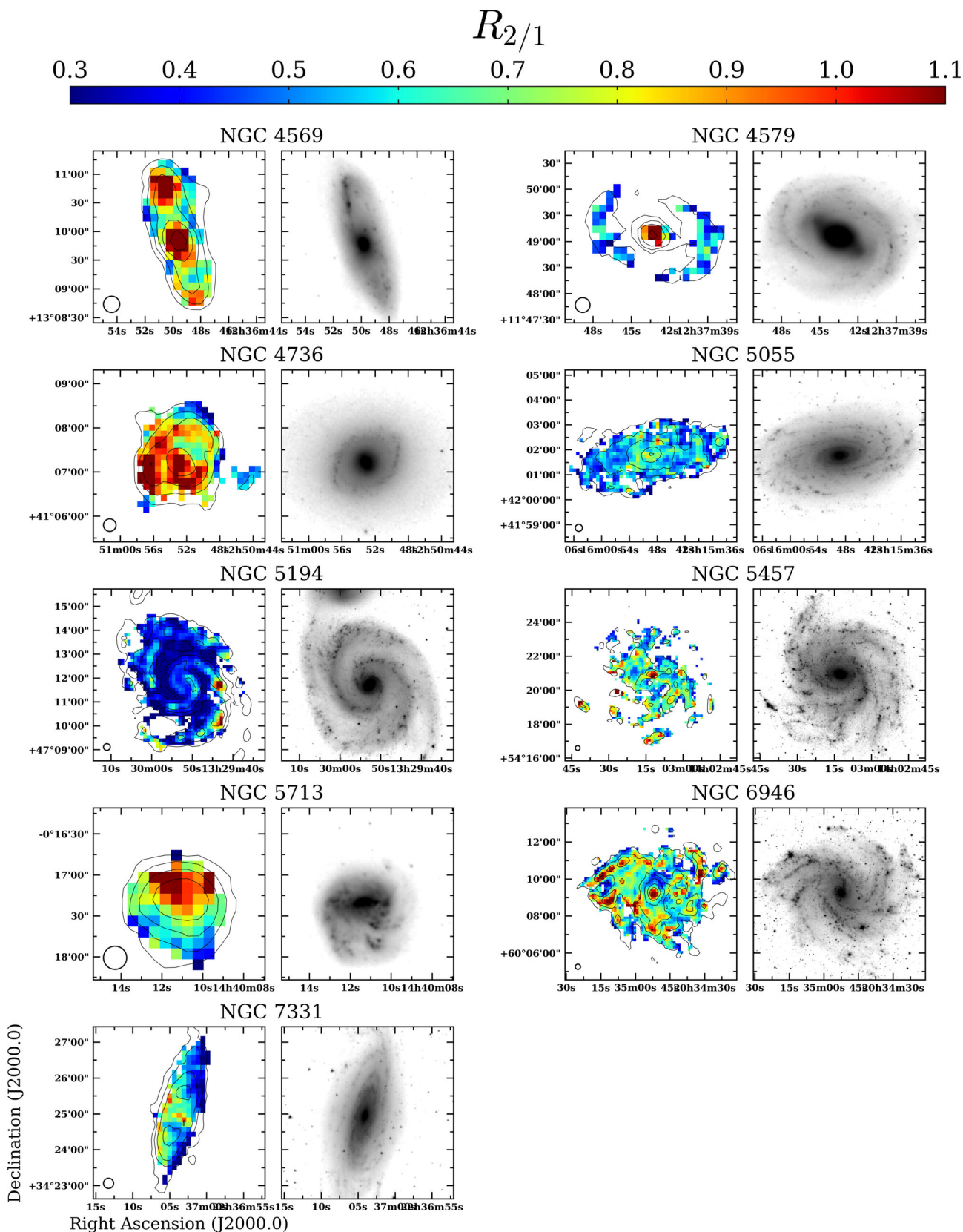


Fig. 2. (Continued)

Table 2. Statistics of $R_{2/1}$ and properties of the samples.*

| Galaxy | $Q_2(R_{2/1})$ | $\overline{R_{2/1}}$ | $\sigma(R_{2/1})$ | $\overline{\Sigma_{\text{mol}}}$ [$M_{\odot} \text{ pc}^{-2}$] | $\overline{\Sigma_{\text{SFR}}}$ [$10^{-2} M_{\odot} \text{ yr}^{-1} \text{ kpc}^{-2}$] | $\overline{\tau_{\text{dep}}}$ [Gyr] | $\overline{I_{70 \mu\text{m}}}/\overline{I_{160 \mu\text{m}}}$ |
|----------|-------------------|----------------------|-------------------|---|--|---|--|
| | (1) | (2) | (3) | (4) | (5) | (6) | (7) |
| All | 0.61 | 0.66 | 0.19 | – | – | – | – |
| NGC 337 | – [†] | – [†] | – [†] | – [†] | – [†] | – [†] | – [†] |
| NGC 628 | 0.54 | 0.54 | 0.14 | 17.5 | 0.962 | 1.82 | 0.363 |
| NGC 2146 | 0.66 | 0.73 | 0.23 | 113 | 27.9 | 0.406 | 1.22 |
| NGC 2798 | 0.99 | 1.0 | 0.33 | 44.0 | 17.8 | 0.248 | 1.45 |
| NGC 2841 | 0.51 | 0.50 | 0.12 | 4.34 | 0.287 | 1.51 | 0.210 |
| NGC 2903 | 0.59 | 0.62 | 0.11 | 21.8 | 1.93 | 1.13 | – [†] |
| NGC 2976 | 0.67 | 0.67 | 0.20 | 3.13 | 0.527 | 0.594 | 0.483 |
| NGC 3034 | 0.56 | 0.67 | 0.15 | 23.2 | 3.75 | 0.617 | 1.43 |
| NGC 3077 | – [†] | – [†] | – [†] | – [†] | – [†] | – [†] | – [†] |
| NGC 3184 | 0.55 | 0.56 | 0.14 | 14.5 | 0.756 | 1.91 | 0.307 |
| NGC 3198 | 0.46 | 0.47 | 0.10 | 6.37 | 0.915 | 0.697 | 0.493 |
| NGC 3351 | 0.48 | 0.73 | 0.21 | 19.4 | 3.20 | 0.608 | 0.765 |
| NGC 3521 | 0.61 | 0.63 | 0.12 | 31.2 | 2.17 | 1.43 | 0.423 |
| NGC 3627 | 0.46 | 0.46 | 0.10 | 39.0 | 2.96 | 1.32 | 0.543 |
| NGC 3938 | 0.56 | 0.56 | 0.11 | 20.5 | 1.43 | 1.44 | 0.409 |
| NGC 4214 | – [†] | – [†] | – [†] | – [†] | – [†] | – [†] | – [†] |
| NGC 4254 | 0.70 | 0.72 | 0.17 | 39.8 | 3.27 | 1.21 | 0.483 |
| NGC 4321 | 0.76 | 0.83 | 0.18 | 26.7 | 2.00 | 1.33 | 0.421 |
| NGC 4536 | 0.79 | 0.84 | 0.24 | 54.7 | 11.5 | 0.474 | 1.18 |
| NGC 4559 | – [†] | – [†] | – [†] | – [†] | – [†] | – [†] | – [†] |
| NGC 4569 | 0.76 | 0.89 | 0.25 | 27.5 | 1.63 | 1.69 | 0.420 |
| NGC 4579 | 0.50 | 0.63 | 0.20 | 20.1 | 0.890 | 2.25 | 0.396 |
| NGC 4736 | 0.84 | 0.88 | 0.24 | 20.8 | 2.90 | 0.718 | 0.870 |
| NGC 5055 | 0.54 | 0.56 | 0.11 | 18.2 | 0.87 | 2.11 | 0.330 |
| NGC 5194 | 0.40 [§] | 0.41 [§] | 0.16 [§] | – | 2.98 | – | 0.436 |
| NGC 5457 | 0.62 | 0.64 | 0.18 | 15.3 | 0.89 | 1.72 | 0.336 |
| NGC 5713 | 0.72 | 0.80 | 0.24 | 61.3 | 9.35 | 0.656 | 0.804 |
| NGC 6946 | 0.67 | 0.71 | 0.17 | 29.6 | 1.85 | 1.60 | 0.491 |
| NGC 7331 | 0.53 | 0.55 | 0.17 | 18.3 | 1.11 | 1.65 | 0.426 |

* (1) Median of $R_{2/1}$. (2) Mean of $R_{2/1}$ weighted by integrated intensity of $^{12}\text{CO}(J = 1-0)$ averaged over the pixels where $R_{2/1}$ is significantly measured (cf. figure 2). (3) Standard deviation of $R_{2/1}$. (4)–(5) Mean surface density of molecular gas and SFR. The areas used to derive these means are the same as column (2). (6) Mean depletion time derived as total molecular gas mass over total SFR within the area used in column (2). (7) Mean IR color derived as total luminosity of $70 \mu\text{m}$ over that of $160 \mu\text{m}$ within the area used in column (2).

[†] There are few or no pixels to measure $R_{2/1}$.

[‡] Archival data is not available.

[§] There may be a calibration error of the CO data.

^{||} Not derived due to the possibility of calibration error.

3.2 Effects of $R_{2/1}$ on molecular gas mass derived from $^{12}\text{CO}(J = 2-1)$

As effects originating from the assumption that $R_{2/1}$ is a constant, we report on how molecular gas mass is underestimated or overestimated and how the scatter of molecular gas surface density within a galaxy changes. We adopted the standard CO-to- H_2 conversion factor X_{CO} of $2.0 \times 10^{20} \text{ cm}^{-2} (\text{K km s}^{-1})^{-1}$ (Bolatto et al. 2013) for the entire area of all galaxies based on the widely used method.

The top panel of figure 5 shows how the total molecular gas mass within a galaxy changes (rate of change in total molecular gas mass; $\Delta M_{\text{mol}}^{\text{tot}}$) when the molecular

gas mass is derived from $^{12}\text{CO}(J = 2-1)$ with an $R_{2/1}$ of 0.7 compared with the case when $M_{\text{mol}}^{\text{tot}}$ is derived from $\text{CO}(J = 1-0)$. For instance, $\Delta M_{\text{mol}}^{\text{tot}} = -20\%$ indicates that the total molecular gas mass derived from $^{12}\text{CO}(J = 2-1)$ is underestimated by 20%. NGC 337, NGC 3077, NGC 4214, and NGC 4559 are omitted because $R_{2/1}$ cannot be significantly measured in most positions in these galaxies (figure 2), and NGC 5194 is omitted due to the possibility of the calibration problem mentioned in subsection 3.1.

As $\overline{R_{2/1}}$ deviates from 0.7 (table 2), the total molecular gas mass within a galaxy is underestimated or

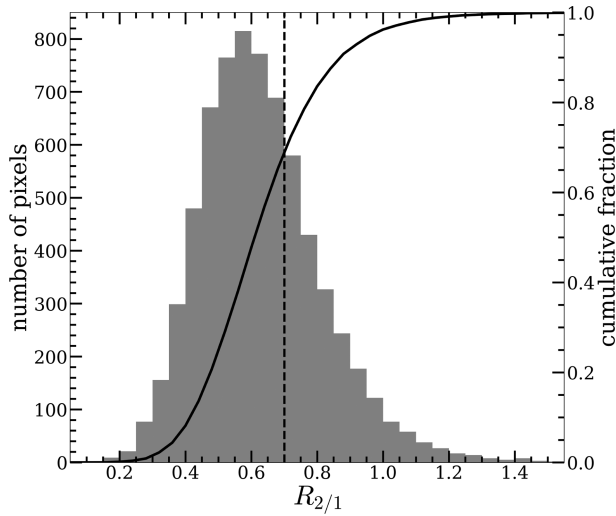


Fig. 3. Histogram of $R_{2/1}$ for all pixels of all galaxies. The solid line shows the cumulative distribution function and the dashed line indicates $R_{2/1} = 0.7$.

overestimated when the molecular gas mass is derived from $^{12}\text{CO}(J = 2-1)$ assuming a constant $R_{2/1}$ of 0.7. For instance, the total molecular gas mass is underestimated by $\sim 30\%$ for galaxies that show low $\overline{R_{2/1}}$ ($\lesssim 0.50$; e.g., NGC 2841, NGC 3198). Further, it is overestimated by $\sim 30\%$ when $\overline{R_{2/1}}$ is high ($\gtrsim 0.9$; e.g., NGC 2798, NGC 4569, NGC 4736). For the most deviated galaxy, the molecular gas mass is underestimated by $\sim 35\%$ in NGC 3627.

The middle panel of figure 5 shows the change rate of the standard deviation for $\log \Sigma_{\text{mol}}$, $\Delta[\sigma(\log \Sigma_{\text{mol}})]$, in each galaxy when $R_{2/1}$ is assumed to be the constant. $\Delta[\sigma(\log \Sigma_{\text{mol}})]$ is positive for all galaxies and exceeds 30% in some galaxies (NGC 628, NGC 2798, NGC 2976, NGC 3351, NGC 5713, and NGC 7331), and the highest one reaches 120% (NGC 2798). When the scatter of $R_{2/1}$, $\sigma(R_{2/1})$, is relatively large ($\gtrsim 0.2$) or when $\overline{R_{2/1}}$ deviates from 0.7, $\Delta[\sigma(\log \Sigma_{\text{mol}})]$ tends to be large. In contrast, when $\sigma(R_{2/1})$ is small, $\Delta[\sigma(\log \Sigma_{\text{mol}})]$ is also small (e.g., NGC 3627). These results indicate that not only the total molecular gas mass but also molecular gas surface density and its relevant quantities from position to position are misinterpreted by the assumption of constant $R_{2/1}$. This becomes an issue when spatially resolved data are used, which has been the standard recently.

3.3 Effects of $R_{2/1}$ on the Kennicutt–Schmidt relation derived from $^{12}\text{CO}(J = 2-1)$

Next, we investigate how the Kennicutt–Schmidt (K–S) relation (Schmidt 1959; Kennicutt 1989) changes when the molecular gas surface density is derived from $^{12}\text{CO}(J = 2-1)$ and a fixed $R_{2/1}$ compare with that

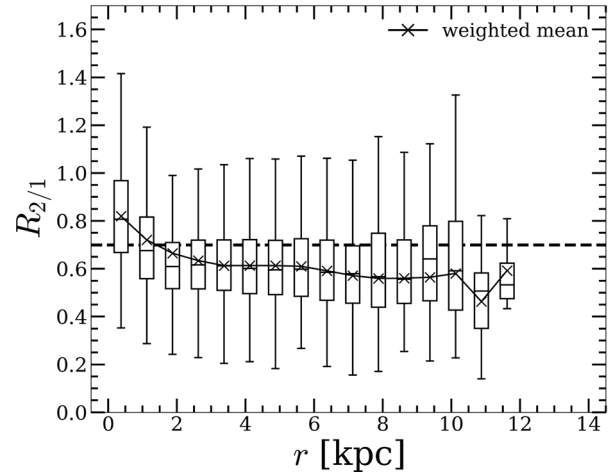
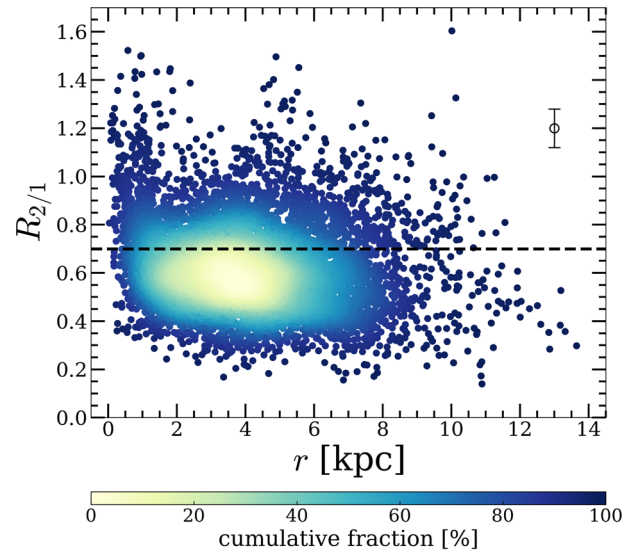


Fig. 4. Radial distribution of $R_{2/1}$ for all galaxies. The dashed line in the both panels indicates $R_{2/1} = 0.7$. (Top) Scatter plot of $R_{2/1}$ against the galactocentric radius. The colors indicate the cumulative fraction of data. The typical error of $R_{2/1}$ is shown on the top right with the open circle marker. (Bottom) Box plot for the top panel. Each bin is 0.75 kpc in width. The cross markers show mean $R_{2/1}$ in a bin weighted by $^{12}\text{CO}(J = 1-0)$ integrated intensity. The upper whisker extends up to the maximum value and the lower whisker extends down to the minimum value in each bin unless the maximum value is less than $Q_3 + 1.5\text{IQR}$ and the minimum value is larger than $Q_1 - 1.5\text{IQR}$, where Q_1 is the 25th percentile, Q_3 is the 75th percentile, and IQR is the interquartile range defined as $Q_3 - Q_1$. Otherwise, the upper whisker extends up to $Q_3 + 1.5\text{IQR}$ and the lower whisker extends down to $Q_1 - 1.5\text{IQR}$ without outliers for simplicity. (Color online)

derived from $^{12}\text{CO}(J = 1-0)$. The molecular K–S relation is described as

$$\log \left(\frac{\Sigma_{\text{SFR}}}{M_{\odot} \text{ yr}^{-1} \text{ kpc}^{-2}} \right) = N \log \left(\frac{\Sigma_{\text{mol}}}{M_{\odot} \text{ pc}^{-2}} \right) + A, \quad (4)$$

where N is the index and A is the intercept on the double-logarithmic plot. Several studies have suggested that this

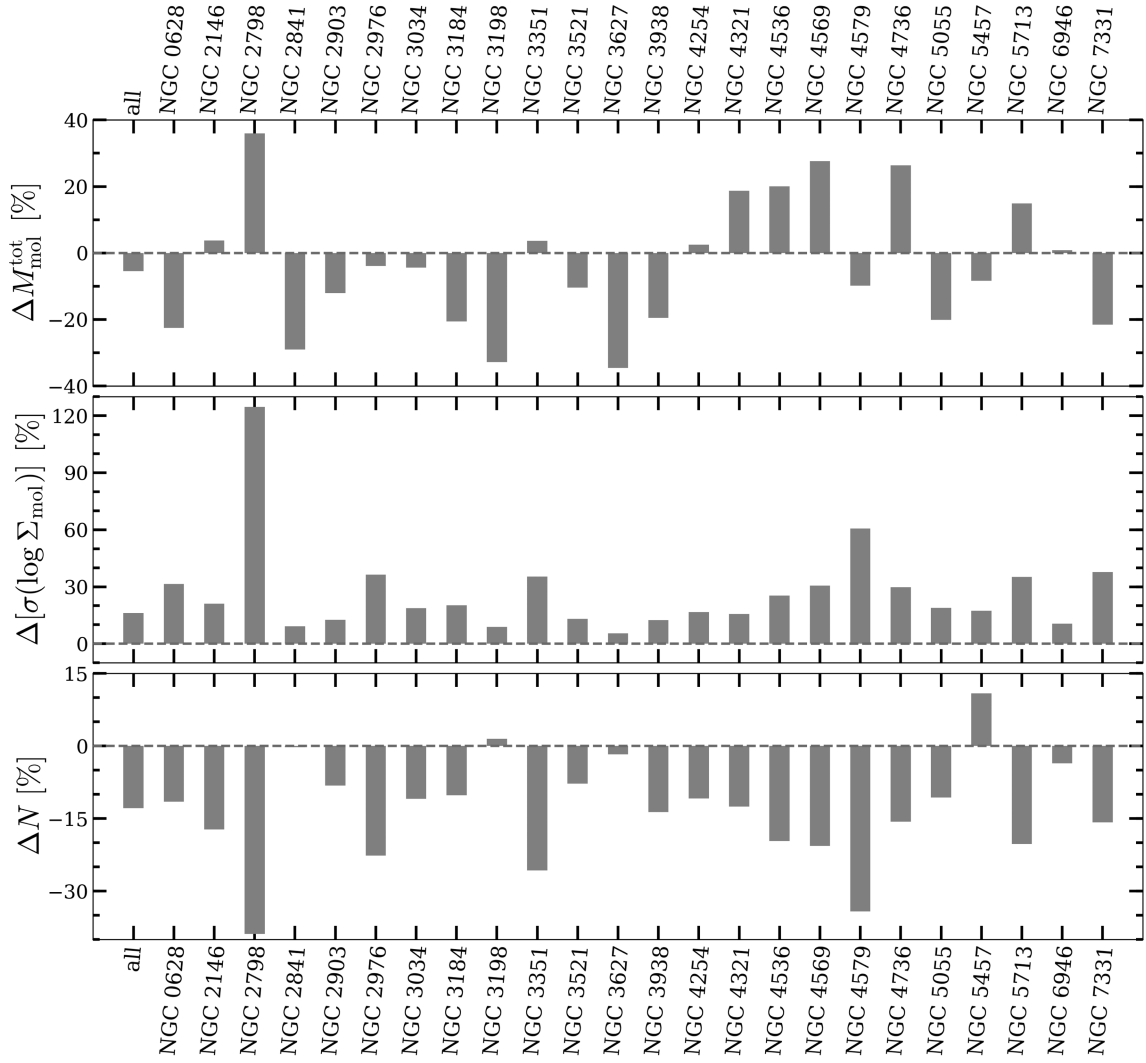


Fig. 5. Rate of change in the total molecular gas mass $\Delta M_{\text{mol}}^{\text{tot}}$ (top), standard deviation of molecular gas surface density $\Delta[\sigma(\log \Sigma_{\text{mol}})]$ (middle), and index of the Kennicutt–Schmidt relation ΔN (bottom) in each galaxy.

relation, in particular N , reflects the processes of star formation in galaxies (e.g., Elmegreen 2002; Krumholz & McKee 2005; Komugi et al. 2006; Tan 2010; T. T. Takeuchi in preparation). Therefore, we focused on how N changes in this study.

When the spatial resolution is changed, the result of the K–S relation also changes (Onodera et al. 2010). Thus, we smoothed ^{12}CO cubes and Σ_{SFR} maps so that the spatial resolution is the same value of 1.5 kpc for all galaxies except for NGC 337, NGC 2146, and NGC 5713. Since the original spatial resolution of these three galaxies is larger than 1.5 kpc (table 1), we did not smooth them. We also regridded ^{12}CO cubes and Σ_{SFR} maps to fix spatial sampling (i.e., pixel size) for all galaxies. The pixel size is set to 650 pc, which is slightly smaller than the Nyquist sampling. For convolved and regridded data, pixels whose integrated-intensity S/N did not reach 4.5σ were masked. We made

K–S plots from $^{12}\text{CO}(J = 1-0)$ by adopting the standard X_{CO} of $2.0 \times 10^{20} \text{ cm}^{-2} (\text{K km s}^{-1})^{-1}$ for the entire area of all galaxies according to the widely used method. The K–S plots from $^{12}\text{CO}(J = 2-1)$ were obtained by converting $^{12}\text{CO}(J = 2-1)$ intensity into that of $^{12}\text{CO}(J = 1-0)$ with a constant $R_{2/1}$ of 0.7, which is the same method employed in previous studies of the K–S relation with $^{12}\text{CO}(J = 2-1)$ (e.g., Bigiel et al. 2008).

We fitted the K–S relation with the ordinary least-squares (OLS) bisector method (Isobe et al. 1990) and derived N and A of the relation made with $^{12}\text{CO}(J = 1-0)$ and $^{12}\text{CO}(J = 2-1)$. Indices derived from $^{12}\text{CO}(J = 1-0)$ and $^{12}\text{CO}(J = 2-1)$, hereafter N_{1-0} and N_{2-1} , intercepts from the two ^{12}CO lines (similarly, A_{1-0} and A_{2-1}), and their rates of change (ΔN and ΔA) are listed in table 3. The bottom panel of figure 5 indicates the change rate of the indices; figure 6 shows the correlation plot of N_{2-1} against N_{1-0} . The K–S

Table 3. Fitted parameters of the K–S relation.*

| Galaxy | N_{1-0} (1) | N_{2-1} (2) | ΔN [%] (3) | A_{1-0} (4) | A_{2-1} (5) | ΔA [%] (6) |
|-----------------------|-------------------|-------------------|-----------------------|--------------------|--------------------|-----------------------|
| All | 1.299 ± 0.005 | 1.132 ± 0.004 | −12.8 | -3.537 ± 0.008 | -3.253 ± 0.007 | −8.02 |
| NGC 337 | — | — | — | — | — | — |
| NGC 628 | 1.08 ± 0.03 | 0.96 ± 0.02 | −11.5 | -3.37 ± 0.05 | -3.10 ± 0.04 | −8.05 |
| NGC 2146 [†] | 1.29 ± 0.02 | 1.07 ± 0.02 | −17.2 | -3.24 ± 0.03 | -2.77 ± 0.03 | −14.3 |
| NGC 2798 | 0.95 ± 0.05 | 0.58 ± 0.04 | −38.8 | -2.37 ± 0.06 | -1.81 ± 0.04 | −23.5 |
| NGC 2841 | 0.5 ± 0.1 | 0.5 ± 0.2 | −0.24 | -2.9 ± 0.4 | -2.8 ± 0.4 | −2.87 |
| NGC 2903 | 0.95 ± 0.02 | 0.87 ± 0.02 | −8.18 | -2.99 ± 0.03 | -2.82 ± 0.03 | −5.64 |
| NGC 2976 | 0.99 ± 0.09 | 0.8 ± 0.1 | −22.7 | -2.8 ± 0.2 | -2.7 ± 0.2 | −1.54 |
| NGC 3034 | 1.13 ± 0.03 | 1.01 ± 0.02 | −10.9 | -2.99 ± 0.04 | -2.77 ± 0.04 | −7.27 |
| NGC 3077 | — | — | — | — | — | — |
| NGC 3184 | 1.04 ± 0.04 | 0.93 ± 0.03 | −10.2 | -3.33 ± 0.07 | -3.12 ± 0.05 | −6.21 |
| NGC 3198 | 1.26 ± 0.06 | 1.28 ± 0.06 | 1.48 | -3.06 ± 0.08 | -2.90 ± 0.08 | −5.22 |
| NGC 3351 | 1.81 ± 0.05 | 1.35 ± 0.03 | −25.7 | -4.02 ± 0.07 | -3.34 ± 0.04 | −16.9 |
| NGC 3521 | 0.89 ± 0.02 | 0.82 ± 0.01 | −7.77 | -2.98 ± 0.03 | -2.83 ± 0.02 | −4.98 |
| NGC 3627 | 1.07 ± 0.02 | 1.05 ± 0.02 | −1.73 | -3.23 ± 0.04 | -3.01 ± 0.03 | −6.89 |
| NGC 3938 | 0.78 ± 0.03 | 0.67 ± 0.02 | −13.6 | -2.86 ± 0.05 | -2.65 ± 0.04 | −7.19 |
| NGC 4214 | — | — | — | — | — | — |
| NGC 4254 | 0.98 ± 0.01 | 0.872 ± 0.008 | −10.8 | -3.08 ± 0.02 | -2.93 ± 0.01 | −4.94 |
| NGC 4321 | 0.90 ± 0.01 | 0.79 ± 0.01 | −12.5 | -2.98 ± 0.02 | -2.87 ± 0.02 | −3.92 |
| NGC 4536 | 0.81 ± 0.04 | 0.65 ± 0.03 | −19.7 | -2.33 ± 0.06 | -2.10 ± 0.03 | −9.81 |
| NGC 4559 | — | — | — | — | — | — |
| NGC 4569 | 1.15 ± 0.02 | 0.91 ± 0.02 | −20.6 | -3.46 ± 0.04 | -3.19 ± 0.04 | −7.89 |
| NGC 4579 | 1.31 ± 0.04 | 0.86 ± 0.03 | −34.2 | -3.78 ± 0.06 | -3.12 ± 0.05 | −17.5 |
| NGC 4736 | 1.13 ± 0.05 | 0.96 ± 0.03 | −15.7 | -3.04 ± 0.07 | -2.82 ± 0.05 | −7.16 |
| NGC 5055 | 0.969 ± 0.009 | 0.866 ± 0.007 | −10.6 | -3.28 ± 0.02 | -3.04 ± 0.01 | −7.36 |
| NGC 5457 | 1.21 ± 0.04 | 1.35 ± 0.03 | 10.9 | -3.55 ± 0.06 | -3.58 ± 0.04 | 1.07 |
| NGC 5713 [†] | 1.25 ± 0.03 | 0.99 ± 0.01 | −20.2 | -3.28 ± 0.05 | -2.87 ± 0.02 | −12.5 |
| NGC 6946 | 1.24 ± 0.02 | 1.19 ± 0.02 | −3.56 | -3.58 ± 0.03 | -3.49 ± 0.03 | −2.52 |
| NGC 7331 | 1.07 ± 0.02 | 0.90 ± 0.01 | −15.8 | -3.31 ± 0.03 | -2.99 ± 0.02 | −9.7 |

* (1) Index of the K–S relation derived from $^{12}\text{CO}(J = 1-0)$. (2) Index of the K–S relation derived from $^{12}\text{CO}(J = 2-1)$ and a constant $R_{2/1}$ of 0.7. (3) Change rate of index. (4) Intercept of the K–S relation derived from $^{12}\text{CO}(J = 1-0)$. (5) Intercept of the K–S relation derived from $^{12}\text{CO}(J = 2-1)$ and a constant $R_{2/1}$ of 0.7. (6) Change rate of intercept.

[†] The spatial resolution is different from 1.5 kpc (cf. table 1).

plots of each galaxy are shown in figure 7. We could not fit the K–S relation for NGC 337, NGC 3077, NGC 4214, and NGC 4559 because the number of pixels at which $R_{2/1}$ is significantly measured is not sufficient. Therefore, these four galaxies were excluded from the K–S relation of all galaxies compiled in the samples (the last panel in figure 7).

We find that indices decrease typically by 10%–20%, up to 39%, when the relation is derived from $^{12}\text{CO}(J = 2-1)$ with constant $R_{2/1} = 0.7$ in 17 galaxies. The K–S relation using molecular gas surface density derived by this method produces a lower index than that derived by $^{12}\text{CO}(J = 1-0)$ for most galaxies. This tendency is the same as Momose et al. (2013), which discussed the discrepancy between their super-linear slope of the K–S relation derived by $^{12}\text{CO}(J = 1-0)$ and the linear slope derived by $^{12}\text{CO}(J = 2-1)$ reported in Bigiel et al. (2008). A significant change ($\Delta N < -20\%$) of the index is shown in NGC 2798, NGC 2976, and NGC 3351. In these galaxies,

$\sigma(R_{2/1})$ within a galaxy tends to be relatively larger than others (table 2). When the variation of $R_{2/1}$ in a galaxy is small (e.g., NGC 3198, NGC 3627), ΔN is small ($|\Delta N| \lesssim 2\%$). The differences of the K–S relation for all sample galaxies also shows a lower index ($\Delta N = -13\%$).

We interpret these underestimated indices of the K–S relation derived from $^{12}\text{CO}(J = 2-1)$ as follows. $R_{2/1}$ is often higher than 0.7 when Σ_{SFR} and Σ_{mol} are high (the top right on the K–S plot), while $R_{2/1}$ is prone to be lower than 0.7 when Σ_{SFR} and Σ_{mol} are low (the bottom left on the K–S plot). Here, we mean that “ Σ_{mol} ” is derived from $^{12}\text{CO}(J = 1-0)$. As a result, molecular gas surface density derived from $^{12}\text{CO}(J = 2-1)$ with a fixed $R_{2/1}$ of 0.7 is overestimated (data points move to the right in the plot) where Σ_{SFR} and Σ_{mol} are high, and it is underestimated (data points move to the left in the plot) where Σ_{SFR} and Σ_{mol} are low (we examine correlations of $R_{2/1}$, Σ_{SFR} , and Σ_{mol} in subsection 4.1; figures 8 and 9). This becomes prominent

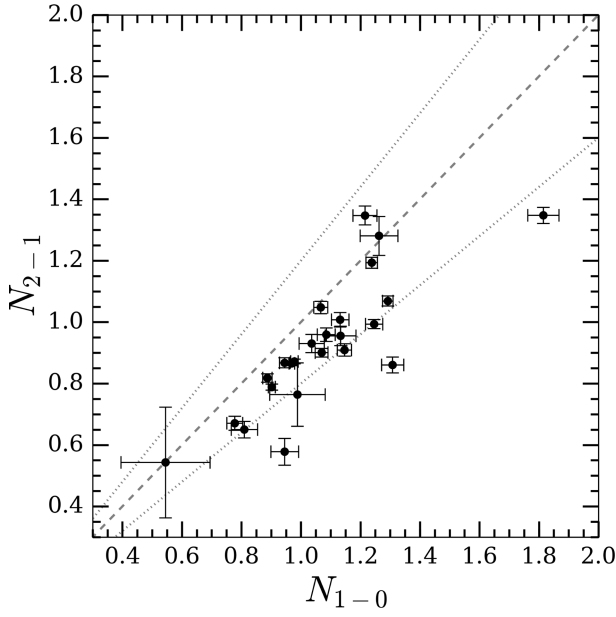


Fig. 6. Indices of the K–S relation derived from $^{12}\text{CO}(J = 2-1)$ with a constant $R_{2/1}$ of 0.7 (N_{2-1}) against that from $^{12}\text{CO}(J = 1-0)$ (N_{1-0}). The diagonal dashed line indicates $N_{2-1} = N_{1-0}$. Dotted lines indicate that N_{2-1} is higher and lower by 20% than N_{1-0} .

in galaxies whose $\sigma(R_{2/1})$ is large, as seen in the plot of NGC 2798, NGC 3351, and NGC 4579 of figure 7. We note that indices are underestimated even if $R_{2/1}$ is assumed as the mean or median of $R_{2/1}$ in a galaxy.

When the K–S relation is derived from higher- J ^{12}CO lines such as $^{12}\text{CO}(J = 3-2)$, the same tendency of lower indices is seen (Morokuma-Matsui & Muraoka 2017). Dense gas tracers also produce nearly linear K–S relations, whereas $^{12}\text{CO}(J = 1-0)$ produces super-linear relations (e.g., Kennicutt 1989; Gao et al. 2007). According to these results, it seems that indices of the K–S relation become low when the relation is derived from the molecular gas, which is more related to star-formation activity. We conclude that the K–S relation, the basic relation of molecular gas with star formation, will be misinterpreted, in addition to total molecular gas within a galaxy and surface density of molecular gas when $^{12}\text{CO}(J = 2-1)$ is used as a molecular gas tracer with a fixed $R_{2/1}$. Previous studies of the K–S relation using molecular gas surface density derived from this method would underestimate their indices.

4 Discussion

4.1 Correlations of $R_{2/1}$ with basic properties of galaxies

To investigate how $R_{2/1}$ changes depending on basic properties of galaxies such as Σ_{SFR} , correlations of $R_{2/1}$ with representative quantities are examined in this subsection.

The spatial resolution and grid spacing are fixed to be 1.5 kpc and 650 pc except for NGC 337, NGC 2146, and NGC 5713, similar to the K–S relation case (these three galaxies were analyzed with their original resolution as shown in table 1).

First, we describe the correlation of $R_{2/1}$ with Σ_{SFR} . The top panel of figure 8 shows the correlation plot of $R_{2/1}$ against Σ_{SFR} for spatially resolved data and integrated data over the pixels where $R_{2/1}$ is significantly measured (table 2, figure 2). The bottom panel of the figure shows the box plot for the top panel binned with 0.2 dex and the mean $R_{2/1}$ weighted by $^{12}\text{CO}(J = 1-0)$ integrated intensity in each bin. The Spearman’s rank correlation coefficients (ρ_s) for the spatially resolved case and the integrated one are 0.47 and 0.51, respectively. Although the scatter is rather large, $Q_2(R_{2/1})$ and $\overline{R_{2/1}}$ in each bin clearly increase from ~ 0.4 to ~ 0.9 as Σ_{SFR} increases. This result is consistent with Koda et al. (2012, 2020), whereas the spatial resolution of the former is approximately twice ours. From this result, the possibilities are as follows: one main physical factor to change $R_{2/1}$ can be star-formation feedback (i.e., high $R_{2/1}$ is a result and high Σ_{SFR} is a cause), or $R_{2/1}$ becomes high because the molecular gas is dense and, as a result, the star-formation rate is high (i.e., high-density condition is a cause and high $R_{2/1}$ and high Σ_{SFR} are results). Otherwise, this correlation might be just mere coincidence.

Second, we investigate the dependence of $R_{2/1}$ on Σ_{mol} as shown in figure 9. Mean Σ_{mol} is derived by the same method as mean Σ_{SFR} . $R_{2/1}$ loosely increases from ~ 0.55 to ~ 0.8 as Σ_{mol} increases according to the bottom panel, while there seems to be no clear tendency according to the scatter plot in the top panel. The ρ_s for the spatially resolved and global result is 0.28 and 0.51, respectively. Since the tendency of $R_{2/1}$ against Σ_{SFR} is clearer than against Σ_{mol} , the lower indices of the K–S relation using molecular gas mass derived from $^{12}\text{CO}(J = 2-1)$ (discussed in subsection 3.3) are mainly due to $R_{2/1}$ fluctuated by Σ_{SFR} rather than Σ_{mol} .

Third, the correlation between $R_{2/1}$ and the depletion time of molecular gas (τ_{dep}) is examined; τ_{dep} is derived from the following equation:

$$\left(\frac{\tau_{\text{dep}}}{\text{yr}}\right) = \left(\frac{\Sigma_{\text{mol}}}{M_{\odot} \text{ pc}^{-2}}\right) / \left(\frac{\Sigma_{\text{SFR}}}{M_{\odot} \text{ yr}^{-1} \text{ pc}^{-2}}\right). \quad (5)$$

Figure 10 shows the relation between $R_{2/1}$ and τ_{dep} in the same way as figure 8. Mean τ_{dep} is derived by dividing the total molecular gas mass by the total SFR within the pixels where $R_{2/1}$ is significantly measured. Both the top and bottom panels show significantly decreased $R_{2/1}$ as τ_{dep} increases. This relation is also consistent with Koda

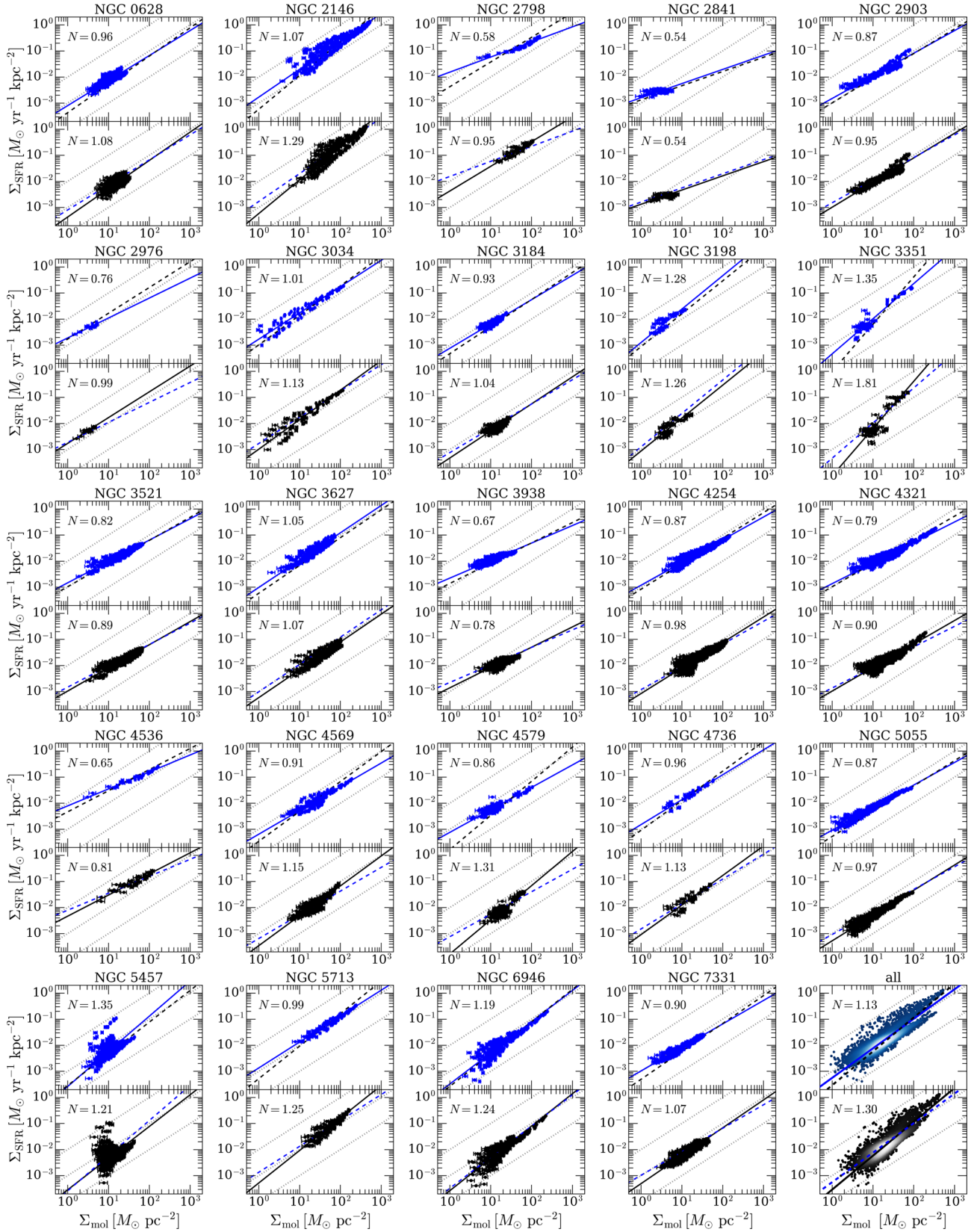


Fig. 7. K-S relation of the sample galaxies derived from $^{12}\text{CO}(J=2-1)$ assuming $R_{2/1} = 0.7$ (top panels, blue plots) and from $^{12}\text{CO}(J=1-0)$ (bottom panels, black plots). The index of each panel is provided on the top left. Solid lines and dashed lines indicate regression lines of the panel and the other panel, respectively. Dotted lines indicate that the depletion time of molecular gas is 10^{-1} Gyr, 10^0 Gyr, and 10^1 Gyr from bottom to top. The K-S plot of all galaxies (excluding NGC 337, NGC 3077, NGC 4214, NGC 4559, and NGC 5194) is shown in the panel at the bottom right corner. (Color online)

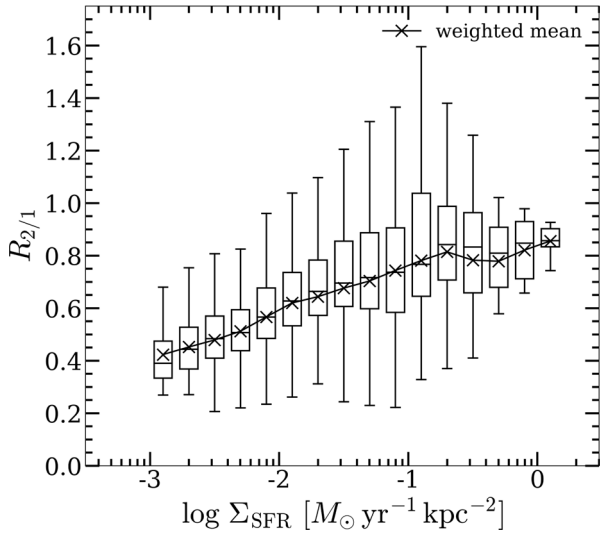
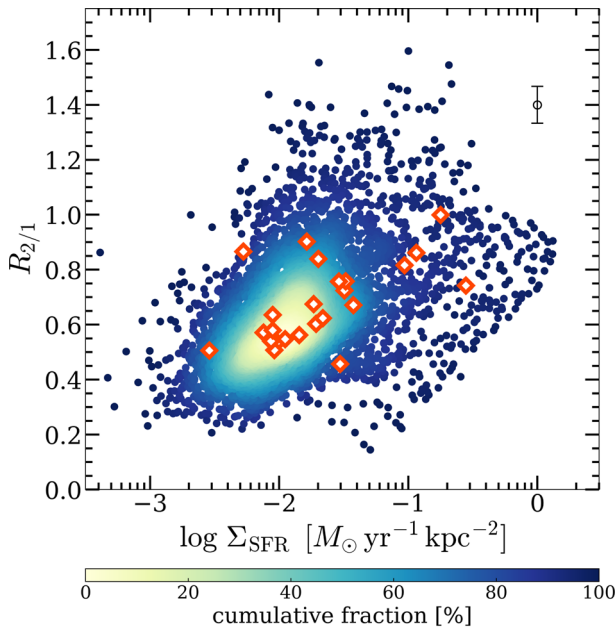


Fig. 8. (Top) Correlation of spatially resolved data (circles) and integrated data over the whole galaxy (open orange diamonds) of $R_{2/1}$ and Σ_{SFR} . The colors indicate the cumulative fraction of data points. The typical error of $R_{2/1}$ is shown on the top right in the panel. The errors in Σ_{SFR} are negligible. (Bottom) Box plot and $\overline{R_{2/1}}$ in each bin (cross markers) for the top panel. The bin width is 0.2 dex. The settings of the box plot are the same as in figure 4. (Color online)

et al. (2012).² The ρ_s for the spatially resolved and integrated case is -0.47 and -0.50 , respectively. $Q_2(R_{2/1})$ and $\overline{R_{2/1}}$ decrease from ~ 1.2 to ~ 0.45 when τ_{dep} increases from ~ 0.1 Gyr to ~ 5 Gyr. Therefore, $R_{2/1}$ may be related to an efficient conversion from molecular gas into stars because of the dense condition (e.g., Muraoka et al. 2016; Yajima et al. 2019). As another possibility, molecular gas is easily

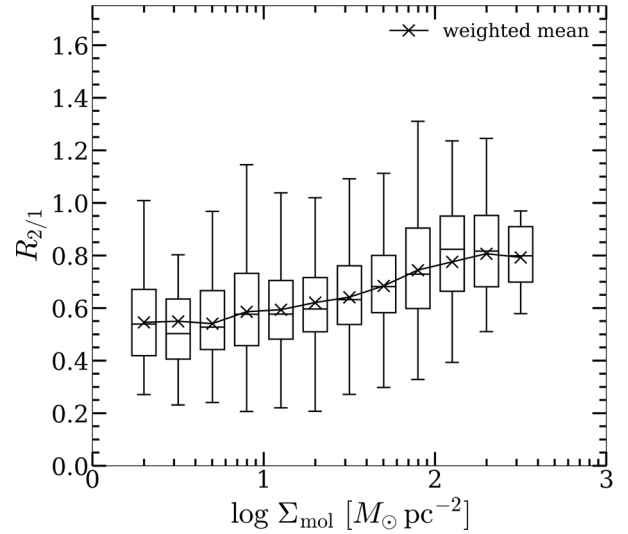
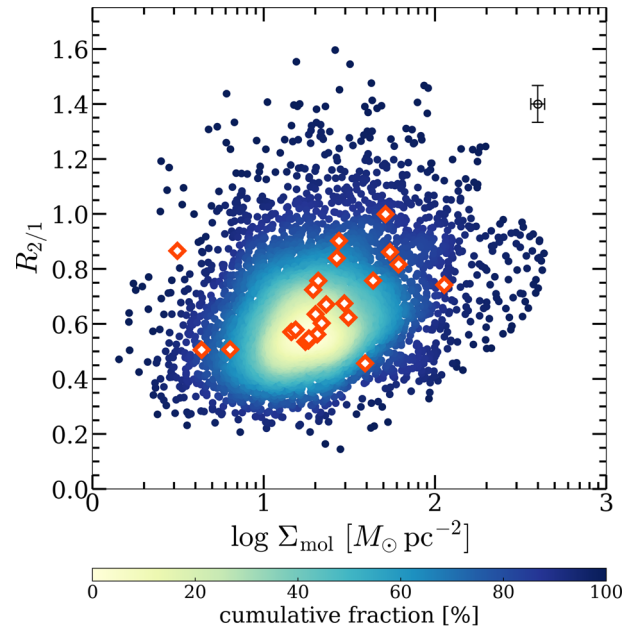


Fig. 9. As figure 8 but for Σ_{mol} . (Color online)

warmed by active star formation (heat source) with poor molecular gas (low heat capacity) when τ_{dep} is short. These possibilities are relevant to the dense or warm conditions of molecular gas likely mentioned in the Σ_{SFR} case.

Finally, the correlation of $R_{2/1}$ with IR color is examined. The IR color is derived from Herschel/PACS $70\ \mu\text{m}$ and $160\ \mu\text{m}$ intensity ratios. Usually, the peak of the spectral energy distribution (SED) for cool dust, which is dominant in ISM, is around the $160\ \mu\text{m}$ band. Therefore, this band selection well reflects the dust temperature, especially in the present case of lacking long-wavelength data for most of the sample galaxies. Cool dust temperature may also be a good probe of ISM conditions. Since there is no archival data of PACS for NGC 2903, we do not derive IR color for this

² Note that the horizontal axis in Koda et al. (2012) is proportional to SFE, which is equivalent to the reciprocal of τ_{dep} .

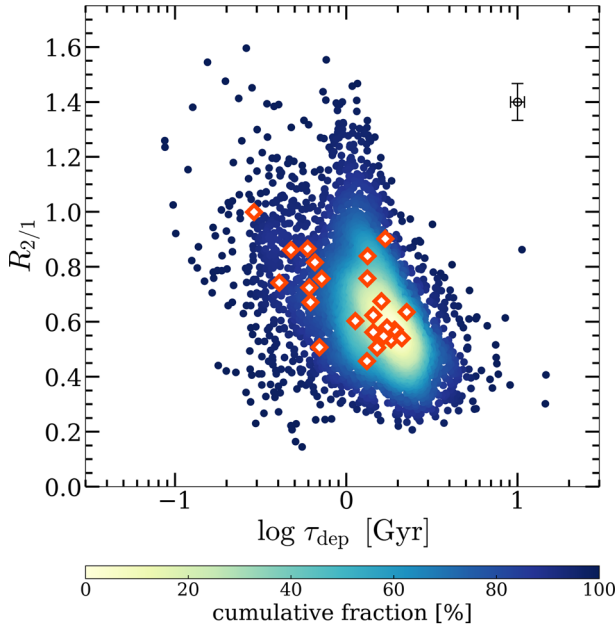


Fig. 10. As figure 8 but for τ_{dep} . (Color online)

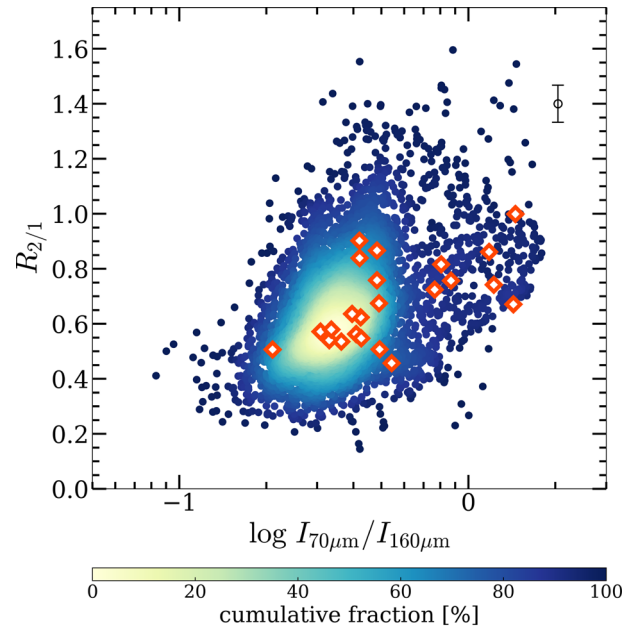


Fig. 11. As figure 8 but for IR color ($I_{70\mu\text{m}}/I_{160\mu\text{m}}$). The errors in IR color are negligible. (Color online)

galaxy. Figure 11 shows the correlation between $R_{2/1}$ and IR color and a box plot in the same manner as figure 8. The mean IR color is derived from the ratio of total intensity, $I_{70\mu\text{m}}$ to $I_{160\mu\text{m}}$, within the pixels where $R_{2/1}$ is significantly measured. The ρ_s of the spatially resolved and integrated case is 0.39 and 0.49. Both $Q_2(R_{2/1})$ and $\overline{R_{2/1}}$ increase from ~ 0.4 to ~ 0.85 as IR color increases (the corresponding dust temperature is from ~ 15 K to ~ 35 K), similarly to the Σ_{SFR} case. The tendency is consistent with Koda et al. (2020). However, the correlation coefficient between $R_{2/1}$ and IR color is higher than that for $R_{2/1}$ and Σ_{SFR} in their paper, whereas it is not higher (0.47 and 0.39) in our results. This difference may originate from far-IR band selection and

sample selection, because their resolution is comparable to ours (their resolution is 1.2 kpc and ours is 1.5 kpc).

4.2 $R_{2/1}$ and physical properties of molecular gas

4.2.1 $R_{2/1}$ and $^{12}\text{CO}(J=1-0)/^{13}\text{CO}(J=1-0)$ ratio

In this subsection we investigate how the properties of molecular gas (such as density and temperature) change $R_{2/1}$. We obtained $^{13}\text{CO}(J=1-0)$ maps of the COMING galaxies in our samples. Therefore, the number density of the molecular gas, $n(\text{H}_2)$, and its kinetic temperature, T_{kin} , can be derived with a non-local thermodynamic equilibrium (non-LTE) analysis with the integrated intensity ratios

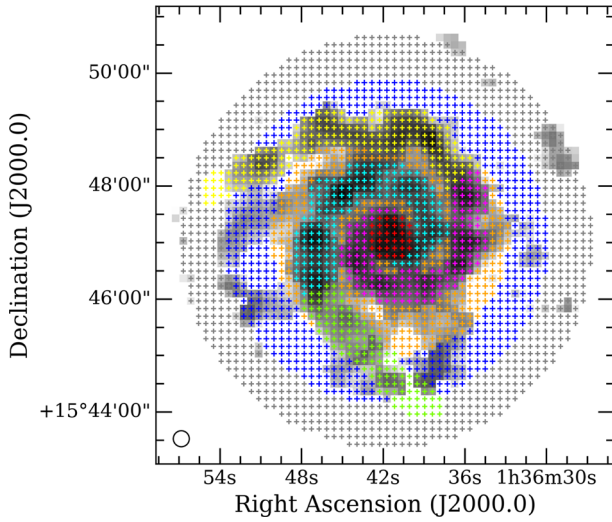


Fig. 12. Regions for spectra stacking in NGC 628: center (red), inner arm 1 (magenta), inner arm 2 (cyan), outer arm 1 (yellow), outer arm 2 (yellow green), inter-arm 1 (orange), inter-arm 2 (blue), and outer disk (gray). Gray scale is the integrated intensity map of $^{12}\text{CO}(J = 2-1)$ obtained by L09. (Color online)

of the three lines (Scoville & Solomon 1974; Goldreich & Kwan 1974).

Since $^{13}\text{CO}(J = 1-0)$ emission is weak compared with ^{12}CO lines, we measured the integrated intensity with the velocity-alignment stacking analysis (Schruba et al. 2011; Morokuma-Matsui et al. 2015) within concentric annuli or galactic structures such as arms and the bar. We determined galactic structures for NGC 628, NGC 2903, and NGC 3627 because the structures of these three galaxies can be clearly seen in the integrated intensity maps of the ^{12}CO lines. The structures determined are shown in figures 12–14. For other galaxies, the regions for spectra stacking are determined as concentric annuli of width $r_{25}/8$. To align spectra along the velocity axis, we used the first-moment maps of H I obtained by The H I Nearby Galaxy Survey (THINGS; Walter et al. 2008) if a galaxy was observed in the survey. The H I first-moment maps enable us to stack spectra even in outer disks. When H I data is not available, the first-moment maps of $^{12}\text{CO}(J = 2-1)$ are used.

Integrated intensities, integrated intensity ratios, and full width at half maximum (FWHM) of stacked spectra are summarized in appendix 2. The 3σ lower limit of the $^{12}\text{CO}(J = 1-0)/^{13}\text{CO}(J = 1-0)$ integrated intensity ratio (hereafter denoted as $R_{12/13}$) is adopted when the S/N of the $^{13}\text{CO}(J = 1-0)$ integrated intensity is lower than 3σ . Prior to the non-LTE analysis, we discuss the relation of $R_{2/1}$ and $R_{12/13}$ as a bare observed quantity. Figure 15 shows the correlation plot of $R_{2/1}$ against $R_{12/13}$.

Regions where the S/N of $^{13}\text{CO}(J = 1-0)$ is poor (derived as only the upper limit of integrated intensity) even with stacking are mainly inter-arms and outer disks. Since the

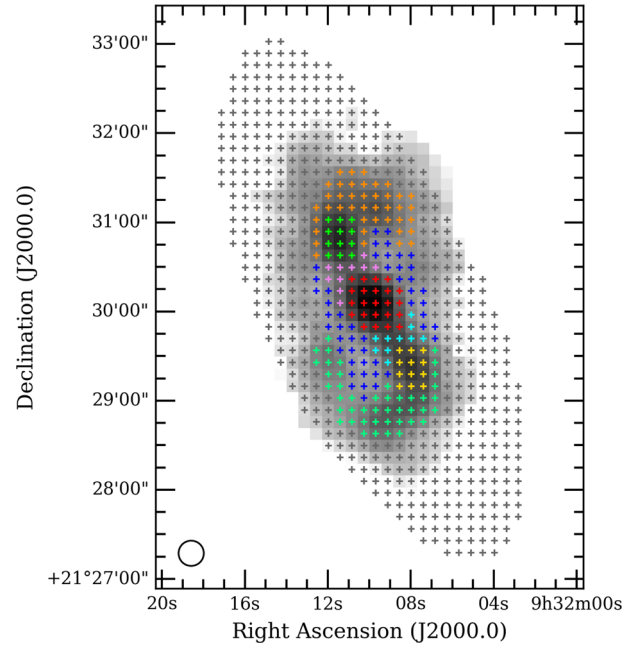


Fig. 13. As figure 12 but for NGC 2903: center (red), northern bar (purple), southern bar (cyan), northern bar end (yellow green), southern bar end (yellow), northern arm (orange), southern arm (mint), inter-arm (blue), and outer disk (gray). The reference for $^{12}\text{CO}(J = 2-1)$ data is the same as figure 12. (Color online)

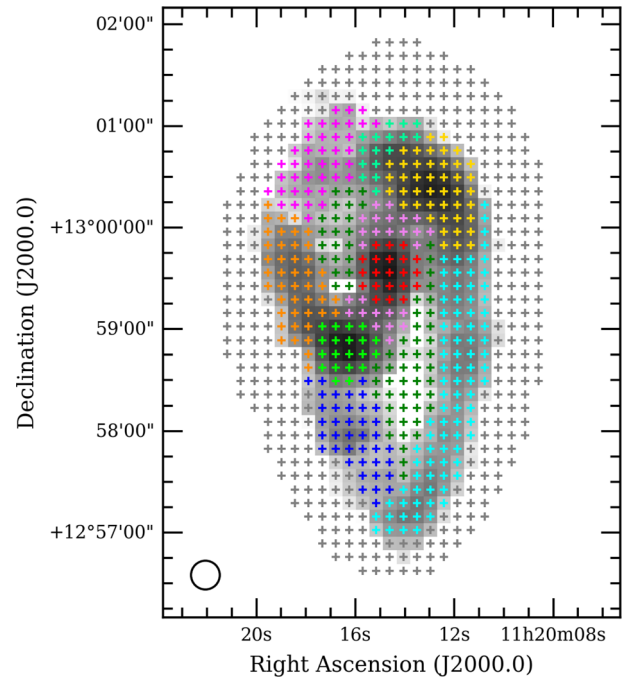


Fig. 14. As figure 12 but for NGC 3627: center (red), bar (purple), northern bar end (yellow), southern bar end (yellow green), western arm (cyan), eastern arm (orange), southern stream (blue), northern offset stream (mint), arm-bar end interacting region (magenta), inter-arm (green), and outer disk (gray). The reference for $^{12}\text{CO}(J = 2-1)$ data is the same as figure 12. (Color online)

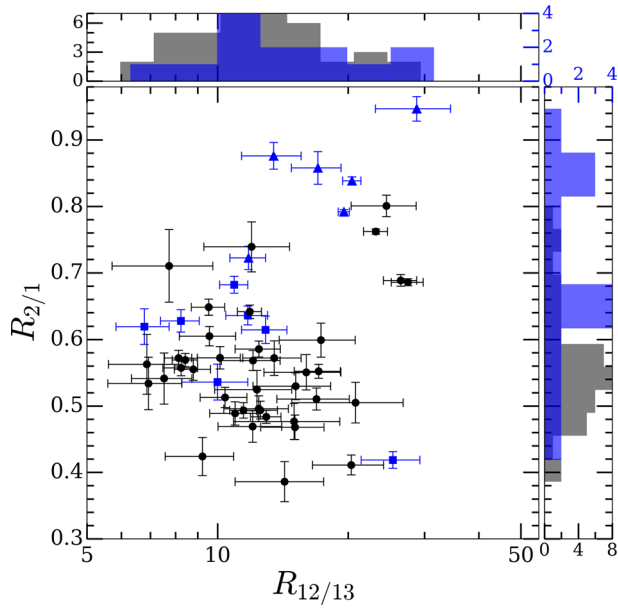


Fig. 15. Correlation of $R_{2/1}$ with $R_{12/13}$ measured from stacked spectra. The black circle markers represent results in disks, blue triangles indicate galactic centers with active star formation (mean Σ_{SFR} in inner $r_{25}/8$ or the region defined as “center” is $>0.1 M_{\odot} \text{ yr}^{-1} \text{ kpc}^{-2}$; NGC 2146, NGC 2903, NGC 3034, NGC 3351, NGC 4536, and NGC 5713), and blue squares indicate galactic centers with quiescent star formation (mean Σ_{SFR} in the region is lower than the value). The black histograms are the results for the disk regions (black plots) and the blue histograms are the results for the galactic centers (blue plots). The colors of the tick labels correspond to the histograms. (Color online)

area where $^{13}\text{CO}(J=1-0)$ is emitted is much smaller than that of ^{12}CO lines in such regions, a different beam-filling factor may be effective, i.e., the line ratio is no longer a probe of molecular gas properties.

In figure 15, it appears that there are two components (or groups): one is with both $R_{2/1}$ and $R_{12/13}$ high, and the other has not so high $R_{2/1}$ ($\lesssim 0.7$) with various $R_{12/13}$ (~ 7 – 20). The former largely includes central regions of galaxies with active star formation (mean Σ_{SFR} within inner $r_{25}/8$ or within the region defined as “center” is higher than $0.1 M_{\odot} \text{ yr}^{-1} \text{ kpc}^{-2}$; NGC 2146, NGC 2903, NGC 3034, NGC 3351, NGC 4536, and NGC 5713). The latter corresponds to galactic disks and centers with quiescent star formation (mean Σ_{SFR} in the region is lower than the value above). The same tendency of decreasing $R_{2/1}$ with increasing $R_{12/13}$ can be seen in the results of another survey (Cormier et al. 2018). It is likely that systematic differences of molecular gas properties between the central region and the disk influencing $R_{2/1}$ and $R_{12/13}$ are seen in the figure. Among galactic structures in disks (arms, inter-arms, bars, etc.), $R_{2/1}$ tends to be relatively low in bars and inter-arms, and high in arms and bar ends, although the contrast of $R_{2/1}$ is low (see the results of stacked spectra for NGC 628, NGC 2903, and NGC 3627 in appendix 2). In addition, the

tendency of $R_{2/1}$ and $R_{12/13}$ among these structures roughly follows the disk-phase feature (i.e., $R_{2/1}$ decreases as $R_{12/13}$ increases). Previous studies of $R_{12/13}$ suggested that high $R_{12/13}$ indicates low $n(\text{H}_2)$ (Meier & Turner 2004), high T_{kin} (Paglione et al. 2001), or low abundance of ^{13}CO due to selective photodissociation (e.g., Davis 2014). Since $R_{2/1}$ is also high in galactic centers with active star formation, both high $n(\text{H}_2)$ and high T_{kin} conditions are possible.

4.2.2 Non-LTE analysis using $R_{2/1}$

To compare $R_{2/1}$ with intrinsic molecular gas properties, $n(\text{H}_2)$ and T_{kin} are derived with non-LTE analysis. In this study, we made use of the one-dimensional non-LTE radiative transfer code RADEX (van der Tak et al. 2007), with settings based on those in Yajima et al. (2019).

Input parameters for calculations are $R_{2/1}$, $R_{12/13}$, the column density of ^{12}CO for all energy levels ($\mathcal{N}_{^{12}\text{CO}}$), that of ^{13}CO ($\mathcal{N}_{^{13}\text{CO}}$), and the FWHM of a GMC’s spectrum (dv). To derive $\mathcal{N}_{^{12}\text{CO}}$ and $\mathcal{N}_{^{13}\text{CO}}$ from the column density of H_2 with observed $I_{^{12}\text{CO}(1-0)}$, the abundance ratios of $[^{12}\text{CO}]/[\text{H}_2]$, $[^{12}\text{CO}]/[^{13}\text{CO}]$, and X_{CO} were adopted as 8.5×10^{-5} (Pineda et al. 2008), 70 (the solar neighborhood value; Milam et al. 2005), and $2.0 \times 10^{20} \text{ cm}^{-2} (\text{K km s}^{-1})^{-1}$ (Bolatto et al. 2013), respectively. For the central region of galaxies, $[^{12}\text{CO}]/[^{13}\text{CO}]$ and X_{CO} were also adopted as 40 and $1.0 \times 10^{20} \text{ cm}^{-2} (\text{K km s}^{-1})^{-1}$, respectively, to reflect the environment of galactic centers (e.g., Meier & Turner 2001; Oka et al. 2001). The photon escape probability was calculated based on the Sobolev approximation (Sobolev 1960).

The FWHM of GMCs, dv , was estimated by assuming that dv in a region is proportional to the FWHM of the stacked spectrum in the region, as described below. This is because molecular gas is a continuous medium and GMCs do not have a rigid boundary. Thus, the internal kinematics of GMCs is likely to be influenced by the dynamics of the surrounding gas (i.e., large-scale dynamics), especially in bar ends and bars where large velocity dispersion can be seen. In addition, since our velocity resolution is 20 km s^{-1} and our spatial resolution is of kiloparsec order, which are much wider than the typical velocity width of GMCs and much larger than their typical size, the FWHM of a stacked spectrum, ΔV , reflects the velocity dispersion among molecular clouds within the beam. This is a good indicator of the large-scale dynamics of molecular gas.

At first, ΔV for a stacked spectrum within the entire disk in each galaxy was measured (hereafter, this ΔV is denoted as ΔV_{disk}) and a dv of 5.0 km s^{-1} was adopted corresponding to ΔV_{disk} . This velocity of 5.0 km s^{-1} as the standard of dv in the entire disk was determined based on the typical FWHM of GMCs in the disk of the Milky Way (e.g., Heyer et al. 2009). Next, the dv of 20 km s^{-1} was

adopted corresponding to ΔV of the galaxy center (hereafter denoted as ΔV_{center}). This 20 km s^{-1} is based on the FWHM of GMCs found in the central region of galaxies and the Milky Way (e.g., Oka et al. 2001; Leroy et al. 2015). Then, the dv for each region (i.e., each annulus or galactic structure) was calculated by linearly interpolating or extrapolating with its ΔV , ΔV_{disk} , and ΔV_{center} . That is, the dv for region i (dv_i) is determined by the following equation:

$$\left(\frac{dv_i}{\text{km s}^{-1}} \right) = a \left(\frac{\Delta V_i}{\text{km s}^{-1}} \right) + b, \quad (6)$$

where

$$a \equiv (20 \text{ km s}^{-1} - 5 \text{ km s}^{-1}) / \left[\left(\frac{\Delta V_{\text{center}}}{\text{km s}^{-1}} \right) - \left(\frac{\Delta V_{\text{disk}}}{\text{km s}^{-1}} \right) \right], \quad (7)$$

$$b \equiv 20 \text{ km s}^{-1} - a \left(\frac{\Delta V_{\text{center}}}{\text{km s}^{-1}} \right), \quad (8)$$

and ΔV_i is the FWHM of the stacked spectrum in the region. The reason dv for the innermost region is fixed to be 20 km s^{-1} is that ΔV_{center} mainly reflects not velocity dispersion on a large scale but the velocity gradient due to the rigid rotation of the galactic disk. High-resolution observations support increasing dv close to the galactic center in inner disks (e.g., Sun et al. 2020). Note that dv does not monotonically increase towards the center in outer disks. Since ΔV in outer disks is almost constant, dv is also constant (see the result for NGC 5055 in appendix 2).

The derived $n(\text{H}_2)$, T_{kin} , and ancillary results of excitation temperature for $^{12}\text{CO}(J=1-0)$, $^{12}\text{CO}(J=2-1)$, and $^{13}\text{CO}(J=1-0)$ ($T_{\text{ex}}^{12(1-0)}$, $T_{\text{ex}}^{12(2-1)}$, $T_{\text{ex}}^{13(1-0)}$), and the optical depth of these lines ($\tau_{12(1-0)}$, $\tau_{12(2-1)}$, $\tau_{13(1-0)}$) are listed in table 4. The errors of $n(\text{H}_2)$ and T_{kin} are derived from the errors of $R_{2/1}$ and $R_{12/13}$. Namely, four pairs of [$n(\text{H}_2)$, T_{kin}] are obtained from $R_{2/1} \pm dR_{2/1}$ and $R_{12/13} \pm dR_{12/13}$ (where $dR_{2/1}$ and $dR_{12/13}$ are the errors of $R_{2/1}$ and $R_{12/13}$, respectively). The errors of $n(\text{H}_2)$, T_{kin} toward the positive direction are adopted as $\max[X_i, i=1, 2, 3, 4] - X_0$, where X_0 is $n(\text{H}_2)$ and T_{kin} is derived from $R_{2/1}$ and $R_{12/13}$, and X_i is $n(\text{H}_2)$ and T_{kin} is derived from $R_{2/1} \pm dR_{2/1}$ and $R_{12/13} \pm dR_{12/13}$. The errors of $n(\text{H}_2)$, T_{kin} toward the negative direction are adopted as $X_0 - \min[X_i, i=1, 2, 3, 4]$. The errors of the other ancillary quantities such as intrinsic intensities and excitation temperature are nearly the same factor as the errors for $n(\text{H}_2)$ and T_{kin} . There are no solutions of the RADEX calculations in several regions. These are caused by the low S/N of $^{13}\text{CO}(J=1-0)$ even with stacking. It is also possible that the one-zone model adopted for RADEX is not valid because the area seen in $^{13}\text{CO}(J=1-0)$ is much smaller

than those seen in $^{12}\text{CO}(J=1-0)$ and $^{12}\text{CO}(J=2-1)$. Based on these RADEX results, we examined the $R_{2/1}$ dependence on $n(\text{H}_2)$ and T_{kin} as shown in figure 16.

There is a clear tendency that $R_{2/1}$ increases with T_{kin} , while $R_{2/1}$ seems to decrease with increasing $n(\text{H}_2)$. The Spearman's rank correlation for $R_{2/1}$ and T_{kin} is 0.67 with a p -value of $\mathcal{O}(10^{-9})$, and that for $R_{2/1}$ and $n(\text{H}_2)$ is -0.36 ; however, it is not statistically significant at a significance level of 5% (p -value is 0.06). In addition, the tendency of increased $R_{2/1}$ with T_{kin} is not changed even when different $[^{12}\text{CO}]/[^{13}\text{CO}]$ and X_{CO} for galactic centers $\{[^{12}\text{CO}]/[^{13}\text{CO}] = 40 \text{ and } X_{\text{CO}} = 1.0 \times 10^{20} \text{ cm}^{-2} (\text{K km s}^{-1})^{-1}\}$ are adopted. The result indicates that the variations of $R_{2/1}$ in galaxies seen at kiloparsec-scale resolutions reflect the temperature of molecular gas. As discussed in subsection 4.1, the positive correlation between $R_{2/1}$ and Σ_{SFR} indicates that $R_{2/1}$ varies depending on T_{kin} or $n(\text{H}_2)$ [high Σ_{SFR} enhances T_{kin} and $R_{2/1}$, or high $n(\text{H}_2)$ induces high Σ_{SFR} and $R_{2/1}$]. Based on the results of the non-LTE analysis, the correlation implies the former case. Radiation feedback from stars warms dust and molecular gas directly and/or dust warms molecular gas; therefore, $R_{2/1}$ becomes high, as suggested by Koda et al. (2020).

Moreover, it seems that there are two phases of molecular gas. One is relatively dense (10^2 – 10^3 cm^{-3}) and cold (5–10 K) with $R_{2/1} \lesssim 0.7$. Its correlation of $R_{2/1}$ with T_{kin} is tight and steep, but there is no clear correlation with $n(\text{H}_2)$. The other is diffuse (20 – 300 cm^{-3}) and warm (30–200 K) with high $R_{2/1}$, and it is loosely correlated with T_{kin} and $n(\text{H}_2)$. The former corresponds to results for disk regions and galactic centers with quiescent star formation (low $R_{2/1}$ and low $R_{12/13}$ indicated by black markers and blue squares in figure 15). The latter is the central regions of galaxies with active star formation (high $R_{2/1}$ and high $R_{12/13}$) indicated by blue triangles in the figure. Differences of molecular gas properties in disks and galactic centers are tested with the Kolmogorov–Smirnov test (i.e., for the black and blue histograms in figure 16). It is confirmed that the hypothesis that T_{kin} and $R_{2/1}$ are the same between the disks and galactic centers is rejected at a significance level of 5%; however, that for $n(\text{H}_2)$ cannot be rejected at the same level (p -value is 0.15). In short, differences of molecular gas phases in disks and centers are clearly seen in $R_{2/1}$ and physical property planes, especially for T_{kin} , at kiloparsec-scale resolutions.

The relation between $R_{2/1}$ and $n(\text{H}_2)$ seems inconsistent with other studies for GMCs (Sakamoto et al. 1994; Nishimura et al. 2015; Peñaloza et al. 2018), although the negative correlation of $R_{2/1}$ with $n(\text{H}_2)$ is not statistically significant. For instance, $R_{2/1}$ is high not only in warm environments but also dense regions such as ridges and filaments in molecular clouds in these studies. The discrepancy is because the spatial scale is quite different between ours

Table 4. Physical properties of molecular gas derived with the non-LTE analysis.*

| Galaxy | Region [†] | $n(\text{H}_2)$ [cm ⁻³] (1) | T_{kin} [K] (2) | $T_{\text{ex}}^{12(1-0)}$ [K] (3) | $T_{\text{ex}}^{12(2-1)}$ [K] (4) | $T_{\text{ex}}^{13(1-0)}$ [K] (5) | $\tau_{12(1-0)}$ (6) | $\tau_{12(2-1)}$ (7) | $\tau_{13(1-0)}$ (8) |
|----------|---------------------|---|--------------------------------|---|---|---|-------------------------|-------------------------|-------------------------|
| NGC 628 | Center | $(1.1^{+0.6}_{-0.3}) \times 10^3$ | $6.5^{+0.9}_{-0.7}$ | 6.3 | 6.1 | 4.4 | 18 | 22 | 0.41 |
| | Inner arm1 | $(1.9^{+1.0}_{-0.6}) \times 10^2$ | $8.2^{+2.5}_{-1.7}$ | 6.9 | 6.1 | 3.4 | 19 | 26 | 0.64 |
| | Inner arm2 | $(2.1^{+0.8}_{-0.5}) \times 10^2$ | $8.8^{+2.2}_{-1.6}$ | 7.4 | 6.6 | 3.5 | 20 | 29 | 0.7 |
| | Outer arm2 | $(6.6^{+4.7}_{-2.2}) \times 10^2$ | $4.8^{+1.3}_{-1.0}$ | 4.5 | 4.0 | 3.3 | 13 | 10 | 0.26 |
| | Inter-arm1 | $(1.8^{+1.9}_{-0.9}) \times 10^2$ | $7.2^{+4.5}_{-2.2}$ | 5.9 | 5.0 | 3.2 | 17 | 20 | 0.49 |
| | Center [‡] | $(8.5^{+3.9}_{-2.3}) \times 10^2$ | $8.5^{+1.9}_{-1.5}$ | 7.8 | 7.2 | 4.9 | 9.8 | 15 | 0.45 |
| NGC 2146 | Center | $(1.7^{+0.6}_{-0.4}) \times 10^1$ | 210^{+110}_{-80} | 14 | 14 | 3.5 | 18 | 40 | 1.6 |
| | Ring1 | $(2.1^{+1.1}_{-0.7}) \times 10^1$ | 69^{+71}_{-29} | 10 | 9.4 | 3.2 | 20 | 38 | 1.2 |
| | Ring2 | $(2.9^{+5.5}_{-2.2}) \times 10^1$ | 23^{+149}_{-13} | 7.0 | 6.0 | 3.0 | 19 | 27 | 0.74 |
| | Center [‡] | — | — | — | — | — | — | — | — |
| NGC 2841 | Ring2 | $(1.2^{+0.2}_{-0.4}) \times 10^3$ | $5.5^{+1.2}_{-0.8}$ | 5.4 | 5.1 | 4.0 | 17 | 17 | 0.36 |
| | Ring3 | $(1.8^{+2.3}_{-0.6}) \times 10^3$ | $5.1^{+0.9}_{-0.9}$ | 5.0 | 4.8 | 4.0 | 15 | 14 | 0.3 |
| | Ring4 | $(1.1^{+1.7}_{-0.5}) \times 10^3$ | $4.8^{+1.6}_{-1.2}$ | 4.7 | 4.3 | 3.6 | 14 | 12 | 0.27 |
| NGC 2903 | Center | $(1.5^{+0.3}_{-0.3}) \times 10^2$ | $14^{+3.0}_{-2.0}$ | 11 | 9.9 | 3.9 | 20 | 38 | 1.1 |
| | Northern bar | $(1.0^{+0.6}_{-0.4}) \times 10^2$ | $13^{+7.0}_{-3.0}$ | 8.5 | 7.5 | 3.4 | 20 | 33 | 0.9 |
| | Southern bar | $(1.1^{+1.2}_{-0.6}) \times 10^2$ | $9.6^{+5.9}_{-3.0}$ | 7.0 | 6.0 | 3.2 | 19 | 27 | 0.68 |
| | Northern bar end | $(3.6^{+0.6}_{-0.5}) \times 10^2$ | $8.8^{+0.9}_{-0.7}$ | 7.9 | 7.4 | 4.0 | 19 | 30 | 0.67 |
| | Southern bar end | $(2.3^{+0.7}_{-0.4}) \times 10^2$ | $8.7^{+1.2}_{-1.1}$ | 7.5 | 6.7 | 3.6 | 20 | 29 | 0.69 |
| | Northern arm | $(4.0^{+1.7}_{-0.8}) \times 10^2$ | $7.8^{+1.0}_{-1.0}$ | 7.1 | 6.6 | 3.8 | 19 | 26 | 0.59 |
| | Southern arm | $(7.3^{+1.5}_{-1.1}) \times 10^2$ | $6.2^{+0.5}_{-0.6}$ | 5.9 | 5.5 | 3.9 | 18 | 20 | 0.42 |
| | Inter-arm | — | — | — | — | — | — | — | — |
| | Outer disk | $(1.2^{+1.1}_{-0.6}) \times 10^2$ | $9.5^{+6.8}_{-3.1}$ | 7.0 | 6.0 | 3.2 | 19 | 26 | 0.63 |
| | Center [‡] | $(6.8^{+4.1}_{-2.9}) \times 10^1$ | 52^{+97}_{-26} | 12 | 11 | 4.1 | 10 | 22 | 1.1 |
| NGC 2976 | Center | — | — | — | — | — | — | — | — |
| | Ring1 | $(5.3^{+8.0}_{-4.1}) \times 10^1$ | 34^{+17}_{-20} | 12 | 11 | 3.6 | 18 | 38 | 1.2 |
| | Ring2 | $(1.3^{+0.9}_{-0.5}) \times 10^2$ | $16^{+11}_{-5.0}$ | 11 | 10 | 3.9 | 19 | 39 | 1.1 |
| | Ring3 | $(4.5^{+2.3}_{-1.7}) \times 10^2$ | $9.6^{+4.0}_{-2.6}$ | 8.8 | 8.4 | 4.5 | 19 | 32 | 0.68 |
| NGC 3034 | Center | $(2.3^{+0.4}_{-0.4}) \times 10^1$ | 95^{+30}_{-19} | 13 | 12 | 3.5 | 18 | 40 | 1.6 |
| | Ring1 | $(1.9^{+0.8}_{-0.5}) \times 10^1$ | 110^{+70}_{-40} | 12 | 11 | 3.4 | 19 | 40 | 1.4 |
| | Ring2 | $(1.8^{+1.0}_{-0.6}) \times 10^1$ | 80^{+66}_{-35} | 10 | 9.3 | 3.2 | 20 | 38 | 1.2 |
| | Center [‡] | — | — | — | — | — | — | — | — |
| NGC 3198 | Center | $(6.0^{+2.6}_{-1.6}) \times 10^2$ | $6.3^{+1.2}_{-1.0}$ | 5.9 | 5.5 | 3.7 | 17 | 19 | 0.42 |
| | Ring1 | $(2.2^{+2.6}_{-1.1}) \times 10^2$ | $7.6^{+5.3}_{-2.5}$ | 6.4 | 5.6 | 3.3 | 18 | 22 | 0.53 |
| | Center [‡] | $(3.7^{+2.0}_{-1.3}) \times 10^2$ | $9.7^{+4.1}_{-2.5}$ | 7.7 | 6.7 | 4.1 | 9.3 | 14 | 0.51 |
| NGC 3351 | Center | $(5.6^{+3.7}_{-2.6}) \times 10^1$ | 48^{+73}_{-20} | 16 | 16 | 4.1 | 18 | 43 | 1.8 |
| | Ring1 | $(3.6^{+5.5}_{-1.5}) \times 10^2$ | $7.6^{+5.1}_{-2.6}$ | 7.0 | 6.4 | 3.7 | 20 | 27 | 0.62 |
| | Ring2 | $(7.2^{+11.0}_{-3.2}) \times 10^2$ | $5.7^{+2.2}_{-1.5}$ | 5.5 | 5.0 | 3.7 | 16 | 17 | 0.36 |
| | Center [‡] | $(2.8^{+3.5}_{-1.3}) \times 10^1$ | 230^{+110}_{-180} | 16 | 16 | 4.2 | 12 | 30 | 1.6 |

Table 4. (Continued)

| Galaxy | Region [†] | $n(\text{H}_2)$ [cm ⁻³] (1) | T_{kin} [K] (2) | $T_{\text{ex}}^{12(1-0)}$ [K] (3) | $T_{\text{ex}}^{12(2-1)}$ [K] (4) | $T_{\text{ex}}^{13(1-0)}$ [K] (5) | $\tau_{12(1-0)}$ (6) | $\tau_{12(2-1)}$ (7) | $\tau_{13(1-0)}$ (8) |
|----------|---------------------------|---|--------------------------------|---|---|---|-------------------------|-------------------------|-------------------------|
| NGC 3521 | Center | $(2.2^{+0.6}_{-0.4}) \times 10^2$ | $9.9^{+1.4}_{-1.2}$ | 8.3 | 7.6 | 3.7 | 20 | 32 | 0.79 |
| | Ring1 | $(2.1^{+0.2}_{-0.2}) \times 10^2$ | $10^{+1.0}_{-1.0}$ | 8.5 | 7.8 | 3.7 | 20 | 33 | 0.81 |
| | Ring2 | $(1.3^{+0.4}_{-0.3}) \times 10^2$ | $10^{+2.0}_{-2.0}$ | 7.6 | 6.6 | 3.3 | 20 | 30 | 0.76 |
| | Ring3 | $(1.6^{+0.7}_{-0.5}) \times 10^2$ | $9.4^{+3.5}_{-2.2}$ | 7.4 | 6.5 | 3.4 | 19 | 28 | 0.71 |
| | Center [‡] | $(1.3^{+0.6}_{-0.4}) \times 10^2$ | $22^{+16}_{-7.0}$ | 10 | 8.9 | 4.0 | 9.8 | 19 | 0.83 |
| NGC 3627 | Center | $(9.5^{+4.3}_{-3.3}) \times 10^1$ | $8.8^{+3.0}_{-1.8}$ | 6.0 | 5.0 | 3.1 | 18 | 21 | 0.54 |
| | Bar | $(1.8^{+0.8}_{-0.6}) \times 10^2$ | $6.9^{+2.0}_{-1.2}$ | 5.6 | 4.8 | 3.2 | 17 | 18 | 0.46 |
| | Northern bar end | $(3.4^{+0.4}_{-0.4}) \times 10^2$ | $6.6^{+0.6}_{-0.5}$ | 6.0 | 5.3 | 3.5 | 18 | 20 | 0.55 |
| | Southern bar end | $(3.9^{+0.8}_{-0.6}) \times 10^2$ | $6.4^{+0.6}_{-0.6}$ | 5.8 | 5.2 | 3.5 | 17 | 19 | 0.45 |
| | Western arm | $(2.8^{+1.0}_{-0.7}) \times 10^2$ | $6.7^{+1.4}_{-1.0}$ | 5.9 | 5.1 | 3.3 | 18 | 20 | 0.48 |
| | Eastern arm | $(6.2^{+1.6}_{-1.4}) \times 10^2$ | $5.7^{+0.8}_{-0.6}$ | 5.4 | 5.0 | 3.6 | 16 | 17 | 0.37 |
| | Offset stream | $(1.7^{+0.7}_{-0.5}) \times 10^2$ | $8.4^{+2.5}_{-1.6}$ | 6.8 | 5.9 | 3.3 | 19 | 26 | 0.64 |
| | Southern arm | $(2.7^{+1.9}_{-1.0}) \times 10^2$ | $6.8^{+2.5}_{-1.6}$ | 6.0 | 5.2 | 3.4 | 18 | 20 | 0.49 |
| | Arm-bar end inter. region | $(7.7^{+10.3}_{-4.8}) \times 10^1$ | $8.7^{+8.8}_{-3.1}$ | 5.4 | 4.5 | 3.0 | 17 | 17 | 0.45 |
| | Center [‡] | $(4.3^{+5.4}_{-2.9}) \times 10^1$ | 31^{+98}_{-17} | 6.1 | 5.1 | 3.2 | 9.1 | 11 | 0.42 |
| NGC 3938 | Center | $(5.9^{+1.4}_{-0.9}) \times 10^2$ | $7.6^{+0.7}_{-0.8}$ | 7.1 | 6.7 | 4.1 | 18 | 25 | 0.51 |
| | Ring1 | $(4.4^{+1.4}_{-0.7}) \times 10^2$ | $7.1^{+1.0}_{-0.8}$ | 6.6 | 6.1 | 3.8 | 19 | 24 | 0.52 |
| | Ring2 | $(2.9^{+1.0}_{-0.7}) \times 10^2$ | $8.0^{+1.4}_{-1.2}$ | 7.0 | 6.4 | 3.6 | 19 | 26 | 0.6 |
| | Ring3 | $(1.8^{+3.2}_{-0.8}) \times 10^3$ | $5.5^{+1.1}_{-0.1}$ | 5.4 | 5.2 | 4.2 | 16 | 16 | 0.3 |
| | Center [‡] | $(4.0^{+1.1}_{-0.8}) \times 10^2$ | $11^{+2.0}_{-2.0}$ | 9.0 | 8.1 | 4.5 | 9.8 | 17 | 0.6 |
| NGC 4536 | Center | $(3.0^{+2.1}_{-1.5}) \times 10^1$ | 95^{+222}_{-54} | 16 | 15 | 3.8 | 18 | 42 | 1.8 |
| | Center [‡] | — | — | — | — | — | — | — | — |
| NGC 4579 | Center | — | — | — | — | — | — | — | — |
| | Ring1 | $(2.4^{+3.1}_{-1.2}) \times 10^2$ | $8.0^{+5.4}_{-2.6}$ | 6.9 | 6.2 | 3.5 | 19 | 26 | 0.62 |
| | Ring2 | $(3.3^{+1.8}_{-0.8}) \times 10^2$ | $7.1^{+1.7}_{-1.5}$ | 6.3 | 5.7 | 3.5 | 18 | 22 | 0.52 |
| | Center [‡] | — | — | — | — | — | — | — | — |
| NGC 5055 | Center | $(2.2^{+0.3}_{-0.3}) \times 10^2$ | $11^{+1.0}_{-1.0}$ | 9.2 | 8.6 | 3.9 | 20 | 35 | 0.87 |
| | Ring1 | $(7.8^{+1.6}_{-1.4}) \times 10^2$ | $6.3^{+0.5}_{-0.4}$ | 6.0 | 5.6 | 4.0 | 18 | 20 | 0.42 |
| | Ring2 | $(3.8^{+0.5}_{-0.4}) \times 10^2$ | $6.3^{+0.5}_{-0.4}$ | 5.8 | 5.1 | 3.4 | 17 | 19 | 0.45 |
| | Ring3 | $(5.8^{+1.8}_{-1.1}) \times 10^2$ | $6.1^{+0.7}_{-0.7}$ | 5.7 | 5.2 | 3.6 | 17 | 18 | 0.41 |
| | Ring4 | $(4.0^{+1.6}_{-0.9}) \times 10^2$ | $6.4^{+1.1}_{-1.0}$ | 5.9 | 5.2 | 3.5 | 17 | 19 | 0.45 |
| | Ring5 | $(3.8^{+5.0}_{-1.7}) \times 10^2$ | $6.3^{+3.2}_{-1.9}$ | 5.7 | 5.1 | 3.4 | 17 | 19 | 0.43 |
| | Ring6 | $(9.1^{+13.0}_{-4.3}) \times 10^2$ | $4.2^{+1.8}_{-1.2}$ | 4.0 | 3.7 | 3.2 | 11 | 7.1 | 0.19 |
| | Center [‡] | $(1.2^{+0.4}_{-0.2}) \times 10^2$ | $24^{+13}_{-6.0}$ | 11 | 9.8 | 4.1 | 10 | 21 | 0.95 |
| NGC 5713 | Center | — | — | — | — | — | — | — | — |
| | Ring1 | — | — | — | — | — | — | — | — |
| | Ring2 | $(1.6^{+5.1}_{-1.2}) \times 10^1$ | 97^{+390}_{-79} | 9.9 | 9.2 | 3.2 | 19 | 37 | 1.1 |
| | Center [‡] | — | — | — | — | — | — | — | — |

Table 4. (Continued)

| Galaxy | Region [†] | $n(\text{H}_2)$ [cm ⁻³] (1) | T_{kin} [K] (2) | $T_{\text{ex}}^{12(1-0)}$ [K] (3) | $T_{\text{ex}}^{12(2-1)}$ [K] (4) | $T_{\text{ex}}^{13(1-0)}$ [K] (5) | $\tau_{12(1-0)}$ (6) | $\tau_{12(2-1)}$ (7) | $\tau_{13(1-0)}$ (8) |
|----------|---------------------|---|--------------------------------|---|---|---|-------------------------|-------------------------|-------------------------|
| NGC 7331 | Center | $(2.0^{+0.6}_{-0.4}) \times 10^2$ | $9.9^{+2.1}_{-1.6}$ | 8.2 | 7.4 | 3.6 | 19 | 31 | 0.77 |
| | Ring1 | $(8.3^{+1.6}_{-1.4}) \times 10^2$ | $6.2^{+0.5}_{-0.3}$ | 6.0 | 5.6 | 4.0 | 18 | 21 | 0.42 |
| | Ring2 | $(8.7^{+2.1}_{-1.8}) \times 10^2$ | $6.0^{+0.5}_{-0.4}$ | 5.8 | 5.4 | 3.9 | 18 | 20 | 0.41 |
| | Ring3 | $(5.3^{+1.8}_{-1.3}) \times 10^2$ | $5.7^{+1.1}_{-0.8}$ | 5.4 | 4.8 | 3.5 | 16 | 16 | 0.38 |
| | Center [‡] | $(9.8^{+5.3}_{-4.1}) \times 10^1$ | $24^{+32}_{-9.0}$ | 9.5 | 8.4 | 3.8 | 10 | 19 | 0.86 |

* (1) Number density of molecular gas. (2) Kinetic temperature of molecular gas. (3) Excitation temperature of $^{12}\text{CO}(J=1-0)$. (4) Same as (3) but for $^{12}\text{CO}(J=2-1)$. (5) Same as (3) but for $^{13}\text{CO}(J=1-0)$. (6) Optical depth of $^{12}\text{CO}(J=1-0)$. (7) Same as (6) but for $^{12}\text{CO}(J=2-1)$. (8) Same as (6) but for $^{13}\text{CO}(J=1-0)$. Results of (1)–(8) are obtained from the one-zone model of RADEX.

[†] In annuli cases, regions of each annulus are named “ring1,” “ring2,” ... in order from the galactic center.

[‡] Adopted X_{CO} and $[^{12}\text{CO}]/[^{13}\text{CO}]$ are different to reflect environments in galactic centers.

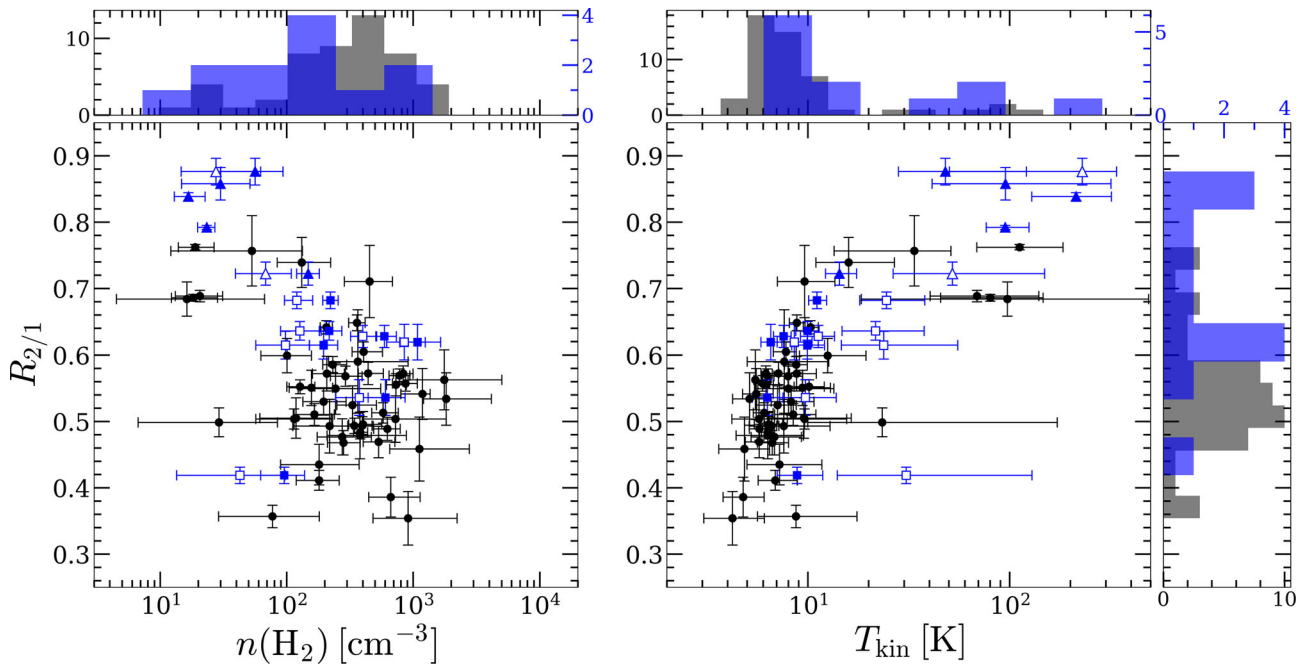


Fig. 16. Correlation of $R_{2/1}$ with $n(\text{H}_2)$ (left) and T_{kin} (right) and their histograms. The black circle markers represent results in disks, and blue filled triangles and squares are galactic centers with active and quiescent star formation, as in figure 15. The blue open markers correspond to central regions in which different $[^{12}\text{CO}]/[^{13}\text{CO}]$ and X_{CO} are adopted. As with the plots, the black histograms are the results of disk regions and the blue histograms are the results of galactic centers. The colors of the tick labels correspond to the histograms. The blue histograms exclude results for which different $[^{12}\text{CO}]/[^{13}\text{CO}]$ and X_{CO} are adopted (open blue markers). (Color online)

(kiloparsec scale) and theirs (order of parsec scale), and the dynamic range of characteristic $n(\text{H}_2)$ is much wider for cloud-scale studies than galactic scales. If observations with such high spatial resolution for galaxies are conducted, high $R_{2/1}$ with high $n(\text{H}_2)$ would appear. Furthermore, observations for molecular clouds in the Milky Way do not contain high- $R_{2/1}$ and high- $R_{12/13}$ environments (common in galactic centers with active star formation) that show warm and diffuse conditions via non-LTE calculations. Thus, the discrepancy possibly originated from the observed

environments (represented on the $R_{2/1}$ – $R_{12/13}$ plane). Related to this, this negative correlation could be produced by the data distribution of the bimodality of molecular gas properties seen in figure 15.

Moreover, studies of molecular gas in other galactic centers support our results of high $R_{2/1}$ with warm diffuse molecular gas seen in central regions with active star formation. For example, Meier, Turner, and Hurt (2000) suggested that there are two phases of molecular gas, warm diffuse layers and cold dense clumps, in the starburst

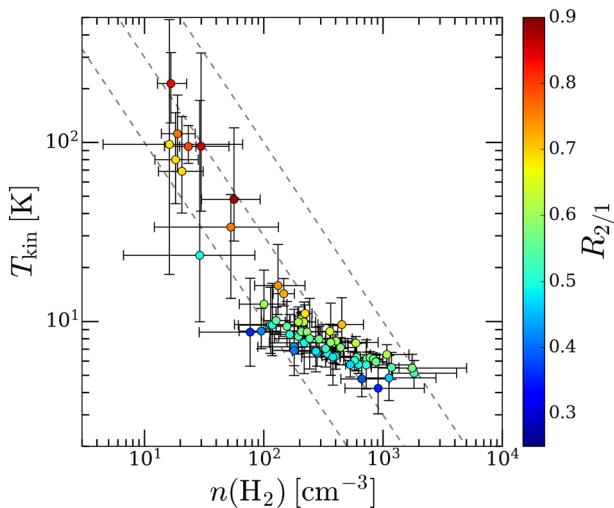


Fig. 17. $R_{2/1}$ distribution on the $T_{\text{kin}}-n(\text{H}_2)$ plot. The dashed lines indicate that pressure divided by k_B is 10^3 K cm^{-3} , $3 \times 10^3 \text{ K cm}^{-3}$, and 10^4 K cm^{-3} from bottom to top. (Color online)

nucleus of IC 342. In addition, low- J ^{12}CO lines, in particular $^{12}\text{CO}(J = 2-1)$, are dominantly emitted in such warm diffuse molecular gas. Israel and Baas (2003) modeled the properties of molecular gas in the center of IC 342 and Maffei 2 (this galaxy also has a modest starburst nucleus) with transitions of ^{12}CO from $J = 1$ to $J = 4$, those of ^{13}CO from $J = 1$ to $J = 3$, and $[\text{C I}]$. Further, they argued for the existence of the warm diffuse molecular gas of $T_{\text{kin}} \sim 100$ – 150 K and $n(\text{H}_2) \sim 10^2 \text{ cm}^{-3}$ associated with the photon-dominated region (PDR), and cold dense clumps of $T_{\text{kin}} \sim 10$ – 20 K and $n(\text{H}_2) \sim 10^3 \text{ cm}^{-3}$. It was also suggested that this warm diffuse molecular gas accounts for approximately two thirds of the total molecular gas. Our results for physical properties with high $R_{2/1}$ reflect such hot diffuse molecular gas related to PDR.

Figure 17 shows the $R_{2/1}$ distribution on the $T_{\text{kin}}-n(\text{H}_2)$ plot. Most of the molecular gas is nearly under a pressure equilibrium of a few 10^3 K cm^{-3} . This figure indicates that both T_{kin} and the pressure of the molecular gas are important for variations of $R_{2/1}$ in galaxies. That is, even when the pressure is so high ($\gtrsim 3 \times 10^3 \text{ K cm}^{-3}$), $R_{2/1}$ is not always high (~ 0.5 – 0.6) as long as T_{kin} is low ($\lesssim 10 \text{ K}$). Similarly, $R_{2/1}$ is not always very high (< 0.8) even when T_{kin} is high ($\gtrsim 30 \text{ K}$) as long as the pressure is not relatively high ($\sim 10^3 \text{ K cm}^{-3}$).

Our results for $R_{2/1}$ and molecular gas properties suggest an issue of molecular gas mass derived from $^{12}\text{CO}(J = 2-1)$ according to fluctuated $R_{2/1}$ and X_{CO} as follows. Some studies reported that X_{CO} is lower in galactic centers, (ultra-)luminous infrared galaxies, and mergers than in disks (i.e., hosting active star formation; e.g., Oka et al. 2001; Narayanan et al. 2011; Papadopoulos et al. 2012;

Sandstrom et al. 2013;³ A. Yasuda et al. in preparation). In these systems, $R_{2/1}$ should be higher than in normal disks considering our results (e.g., figures 4, 8, 11, 16, and 17). In addition, the recent synthetic observation of $^{12}\text{CO}(J = 1-0)$ and $^{12}\text{CO}(J = 2-1)$ in a three-dimensional magneto-hydrodynamics simulation (Gong et al. 2020) shows that X_{CO} is low in environments where $R_{2/1}$ is high. Hence, the molecular gas mass derived from $^{12}\text{CO}(J = 2-1)$ is more overestimated in active star-formation environments when constant $R_{2/1}$ and X_{CO} are adopted because $M_{\text{mol}} \propto I_{^{12}\text{CO}(2-1)} \times X_{\text{CO}}/R_{2/1}$. When $R_{2/1}$ increases and X_{CO} decreases, the fluctuation of $X_{\text{CO}}/R_{2/1}$ is amplified. Based on the reported variations of $X_{\text{CO}}/R_{2/1}$ so far, active star-formation environments lead to more overestimated molecular gas if $^{12}\text{CO}(J = 2-1)$, constant X_{CO} , and fixed $R_{2/1}$ are used compared with the $^{12}\text{CO}(J = 1-0)$ case.

5 Conclusions

We have presented the variations of the $^{12}\text{CO}(J = 2-1)/^{12}\text{CO}(J = 1-0)$ line ratio ($R_{2/1}$) within and among galaxies, the effects of the assumption that $R_{2/1}$ is a constant on the derivation of molecular gas mass, and the properties of molecular gas reflecting variations of $R_{2/1}$ in 24 nearby galaxies on kiloparsec scales. The main conclusions of this paper are as follows:

1. The median and mean $R_{2/1}$ weighted by $^{12}\text{CO}(J = 1-0)$ integrated intensity for spatially resolved data of the galaxies in our samples are 0.61 and 0.66, respectively, with a standard deviation of 0.19. $R_{2/1}$ varies from 0.4 to 0.9 among and within galaxies. While $R_{2/1}$ in the galactic centers (inner $\sim 1 \text{ kpc}$) is typically higher (~ 0.8), the median of $R_{2/1}$ in disks (exterior to $\sim 2 \text{ kpc}$) is nearly constant at 0.60.
2. The total molecular gas mass within a galaxy derived from $^{12}\text{CO}(J = 2-1)$ is underestimated or overestimated by $\sim 20\%$ for most galaxies, and at most by 35% , when $R_{2/1}$ is assumed to be constant at 0.7. In addition, the scatter of molecular gas surface density (Σ_{mol}) by $^{12}\text{CO}(J = 2-1)$ within a galaxy increases in all galaxies. Its change rate exceeds $\sim 30\%$ in some galaxies, and it is 120% in the highest case when a constant $R_{2/1}$ is adopted. This increased scatter of Σ_{mol} is serious for mapping (spatially resolved) observations.
3. The indices of the Kennicutt–Schmidt relation using molecular gas surface density derived from $^{12}\text{CO}(J = 2-1)$ and $R_{2/1} = 0.7$ become lower by 10% – 20% , up to 39% , compared with using $^{12}\text{CO}(J = 1-0)$ for

³ Sandstrom et al. (2013) assumed constant $R_{2/1}$ to derive the molecular gas mass from $^{12}\text{CO}(J = 2-1)$; however, the tendency of lower CO-to- H_2 conversion factors in galactic centers can also be seen in $^{12}\text{CO}(J = 1-0)$ -based studies.

- 17 galaxies out of 24. This is because $R_{2/1}$ tends to be higher than 0.7 when Σ_{SFR} and Σ_{mol} are high, while $R_{2/1}$ is often lower than 0.7 when Σ_{SFR} and Σ_{mol} are low. Underestimated indices are prominent when the scatter of $R_{2/1}$ within a galaxy is large.
4. $R_{2/1}$ has positive correlations with Σ_{SFR} and IR color, and negative correlation with the depletion time of molecular gas. These suggest that $R_{2/1}$ becomes high by warmed molecular gas from stars (stars influence molecular gas properties and $R_{2/1}$). Otherwise, $R_{2/1}$ is high because molecular gas is dense; as a result, star formation is active (molecular gas properties influence star formation activity and $R_{2/1}$). There is no clear tendency between $R_{2/1}$ and Σ_{mol} .
 5. Comparing $R_{2/1}$ with the $^{12}\text{CO}(J=1-0)/^{13}\text{CO}(J=1-0)$ line ratio ($R_{12/13}$) measured within each galactic structure or concentric annulus, there seem to be two components: one is when both $R_{2/1}$ and $R_{12/13}$ are high, and the other is for relatively low $R_{2/1}$ with various $R_{12/13}$. The former corresponds to molecular gas in galactic centers with active star formation (mean Σ_{SFR} within inner $r_{25}/8$ or the region defined as “center” is higher than $0.1 M_{\odot} \text{ yr}^{-1} \text{ kpc}^{-2}$) and the latter corresponds to that in disk regions and centers of galaxies with quiescent star formation (mean Σ_{SFR} in the region is lower than the above value).
 6. According to non-LTE analysis, there is a clear tendency that $R_{2/1}$ increases with T_{kin} ; however, $R_{2/1}$ and $n(\text{H}_2)$ show a rather negative correlation, but it is not statistically significant. This suggests that variations of $R_{2/1}$ on kiloparsec scales imply the temperature of molecular gas. The dependence of $R_{2/1}$ on $n(\text{H}_2)$ would appear when the spatial resolution is higher. Stellar radiation feedback influences molecular gas properties and $R_{2/1}$. The bimodality caused by differences of properties between galactic centers and disks seen on the $R_{2/1}$ – $R_{12/13}$ plane can also be seen on the $R_{2/1}$ – T_{kin} and $R_{2/1}$ – $n(\text{H}_2)$ plots. Molecular gas in the centers is warm and diffuse, and $R_{2/1}$ has relatively loose correlations between T_{kin} and $n(\text{H}_2)$. The disk phase molecular gas is cold and relatively dense, and $R_{2/1}$ is tightly correlated with T_{kin} ; however, it has no relation with $n(\text{H}_2)$.
 7. Not only T_{kin} but also the pressure of molecular gas is important in understanding $R_{2/1}$ variations in galaxies. Namely, even when the pressure is high ($\gtrsim 3 \times 10^3 \text{ K cm}^{-3}$), $R_{2/1}$ is not always high (~ 0.5 – 0.6) as long as T_{kin} is low ($\lesssim 10 \text{ K}$). Likewise, even when T_{kin} is high

($\gtrsim 30 \text{ K}$), $R_{2/1}$ is not always very high (< 0.8) as long as the pressure is not relatively high ($\sim 10^3 \text{ K cm}^{-3}$).

8. Considering variations of the CO-to- H_2 conversion factor X_{CO} , the molecular gas mass in active star-formation environments such as galactic centers and (ultra-)luminous infrared galaxies is more overestimated when it is derived from $^{12}\text{CO}(J=2-1)$ and a constant $R_{2/1}$ of 0.7. This is because molecular gas mass is $\propto I_{^{12}\text{CO}(2-1)} \times X_{\text{CO}}/R_{2/1}$, X_{CO} decreases, and $R_{2/1}$ increases [where $I_{^{12}\text{CO}(2-1)}$ is the integrated intensity of $^{12}\text{CO}(J=2-1)$]. As a result, fluctuations of $X_{\text{CO}}/R_{2/1}$ are amplified.

Acknowledgment

We are grateful to the anonymous referee for their constructive and meaningful comments and suggestions that significantly improved the manuscript. We also thank the staff of Nobeyama Radio Observatory for their help in our observations with the 45 m radio telescope and their continuous efforts to improve the performance of the instruments. This work has been partially supported by JSPS Grants-in-Aid for Scientific Research (17H01110, 18K13593, 19H05076). This work has also been supported in part by the Sumitomo Foundation Fiscal 2018 Grant for Basic Science Research Projects (180923), and the Collaboration Funding of the Institute of Statistical Mathematics “New Development of the Studies on Galaxy Evolution with a Method of Data Science.” The Nobeyama 45 m radio telescope is operated by Nobeyama Radio Observatory, a branch of the National Astronomical Observatory of Japan. This work made use of HERACLES, “The HERA CO-Line Extragalactic Survey” (Leroy et al. 2009). This research has made use of the NASA/IPAC Extragalactic Database, which is operated by the Jet Propulsion Laboratory, California Institute of Technology, under contract with the National Aeronautics and Space Administration. This research has made use of the NASA/IPAC Infrared Science Archive, which is operated by the Jet Propulsion Laboratory, California Institute of Technology, under contract with the National Aeronautics and Space Administration. This research also made use of APLpy, an open-source plotting package for Python (Robitaille & Bressert 2012). We would like to thank Editage (www.editage.com) for English language editing.

Appendix 1 Histograms of $R_{2/1}$ in each galaxy

Figure 18 shows histograms of $R_{2/1}$ in each galaxy for data at the original resolution of $17''$.

Appendix 2 Results of stacked spectra

Table 5 summarizes the parameters of stacked spectra in each region of galaxies.

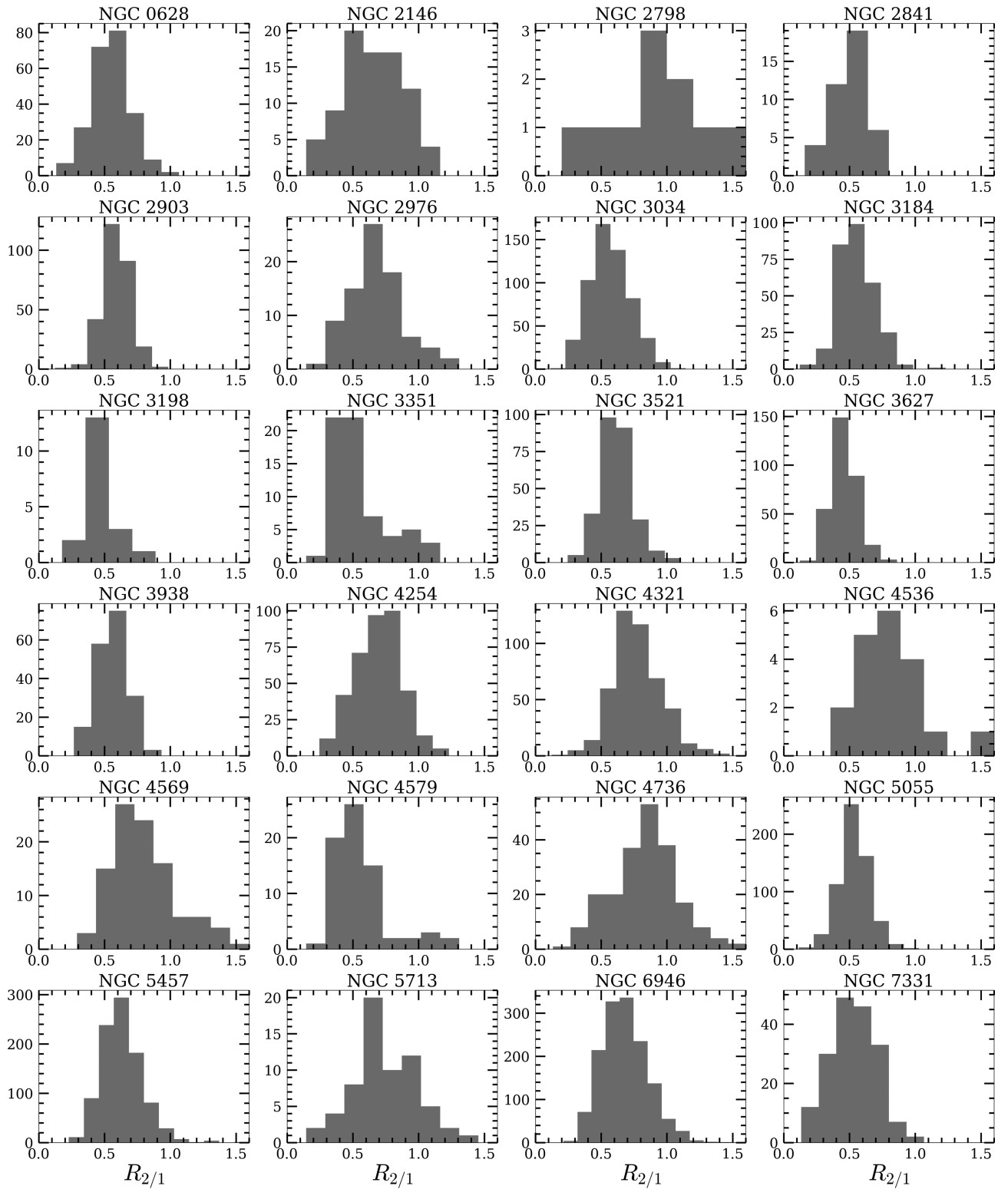


Fig. 18. Histograms of $R_{2/1}$ in each galaxy for original resolution data.

Table 5. Results of the stacking analysis.*

| Galaxy | Region | $I_{12\text{CO}(1-0)}$ [K km s ⁻¹] (1) | $I_{12\text{CO}(2-1)}$ [K km s ⁻¹] (2) | $I_{13\text{CO}(1-0)}$ [K km s ⁻¹] (3) | $R_{2/1}$ (4) | $R_{12/13}$ (5) | ΔV [km s ⁻¹] (6) |
|----------|------------------|--|--|--|------------------|--------------------|--|
| NGC 628 | Center | 6.8 ± 0.3 | 4.23 ± 0.09 | 1.0 ± 0.1 | 0.62 ± 0.03 | 6.8 ± 0.9 | 30 ± 2 |
| | Inner arm1 | 5.3 ± 0.2 | 2.80 ± 0.05 | 0.35 ± 0.07 | 0.53 ± 0.02 | 15.1 ± 3.1 | 28 ± 2 |
| | Inner arm2 | 5.1 ± 0.2 | 2.93 ± 0.05 | 0.38 ± 0.06 | 0.57 ± 0.03 | 13.5 ± 2.1 | 37 ± 2 |
| | Outer arm1 | 3.0 ± 0.2 | 1.92 ± 0.06 | <0.07 | 0.65 ± 0.06 | >41.1 | 28 ± 4 |
| | Outer arm2 | 3.8 ± 0.3 | 1.47 ± 0.06 | 0.27 ± 0.06 | 0.39 ± 0.03 | 14.3 ± 3.3 | 27 ± 3 |
| | Inter-arm1 | 3.1 ± 0.2 | 1.37 ± 0.03 | <0.07 | 0.43 ± 0.03 | >42.9 | 32 ± 4 |
| | Inter-arm2 | 1.6 ± 0.1 | 0.69 ± 0.04 | <0.04 | 0.44 ± 0.04 | >37.3 | 30 ± 5 |
| NGC 2146 | Center | 148 ± 1 | 123.9 ± 0.3 | 7.2 ± 0.4 | 0.839 ± 0.006 | 20.4 ± 1.0 | 202 ± 3 |
| | Ring1 | 52.3 ± 0.6 | 36.0 ± 0.2 | 2.0 ± 0.2 | 0.689 ± 0.009 | 26.4 ± 2.3 | 150 ± 4 |
| | Ring2 | 16.4 ± 0.6 | 8.2 ± 0.1 | <0.18 | 0.50 ± 0.02 | >92.8 | 160 ± 21 |
| | Ring3 | 6.5 ± 0.5 | 3.7 ± 0.2 | <0.2 | 0.57 ± 0.05 | >31.8 | 71 ± 12 |
| NGC 2841 | Ring1 | 5.1 ± 0.2 | 2.2 ± 0.1 | 0.55 ± 0.1 | 0.42 ± 0.03 | 9.2 ± 1.7 | 88 ± 8 |
| | Ring2 | 3.7 ± 0.2 | 2.01 ± 0.09 | 0.49 ± 0.07 | 0.54 ± 0.04 | 7.5 ± 1.2 | 58 ± 6 |
| | Ring3 | 2.4 ± 0.1 | 1.29 ± 0.06 | 0.35 ± 0.06 | 0.53 ± 0.04 | 6.9 ± 1.3 | 59 ± 5 |
| | Ring4 | 1.6 ± 0.1 | 0.74 ± 0.06 | <0.05 | 0.46 ± 0.05 | >30.8 | 67 ± 10 |
| NGC 2903 | Center | 46 ± 1 | 33.5 ± 0.2 | 3.9 ± 0.4 | 0.72 ± 0.02 | 11.8 ± 1.1 | 157 ± 13 |
| | Northern bar | 21.7 ± 0.8 | 13.0 ± 0.3 | 1.3 ± 0.2 | 0.60 ± 0.03 | 17.3 ± 3.4 | 94 ± 7 |
| | Southern bar | 28.0 ± 0.7 | 14.1 ± 0.2 | <0.35 | 0.50 ± 0.02 | >79.2 | 151 ± 4 |
| | Northern bar end | 41.7 ± 0.7 | 27.0 ± 0.2 | 4.4 ± 0.4 | 0.65 ± 0.01 | 9.5 ± 0.8 | 101 ± 3 |
| | Southern bar end | 36.5 ± 0.7 | 21.4 ± 0.2 | 2.9 ± 0.3 | 0.59 ± 0.01 | 12.5 ± 1.5 | 119 ± 4 |
| | Northern arm | 19.7 ± 0.4 | 11.9 ± 0.1 | 2.1 ± 0.3 | 0.61 ± 0.01 | 9.6 ± 1.4 | 65 ± 2 |
| | Southern arm | 18.8 ± 0.5 | 10.4 ± 0.1 | 2.1 ± 0.2 | 0.56 ± 0.02 | 8.8 ± 0.8 | 65 ± 4 |
| | Inter-arm | 13.8 ± 0.4 | 7.0 ± 0.1 | <0.16 | 0.51 ± 0.02 | >85.5 | 82 ± 5 |
| NGC 2976 | Outer disk | 3.9 ± 0.2 | 1.98 ± 0.06 | 0.19 ± 0.05 | 0.51 ± 0.03 | 20.8 ± 6.0 | 53 ± 5 |
| | Center | 3.1 ± 0.3 | 2.61 ± 0.09 | <0.12 | 0.84 ± 0.08 | >24.9 | 33 ± 5 |
| | Ring1 | 2.6 ± 0.2 | 1.98 ± 0.08 | <0.05 | 0.76 ± 0.05 | >49.0 | 31 ± 4 |
| | Ring2 | 3.3 ± 0.1 | 2.41 ± 0.05 | 0.27 ± 0.06 | 0.74 ± 0.04 | 12.0 ± 2.7 | 30 ± 2 |
| | Ring3 | 2.0 ± 0.1 | 1.44 ± 0.07 | 0.26 ± 0.07 | 0.71 ± 0.05 | 7.7 ± 2.0 | 31 ± 4 |
| NGC 3034 | Ring4 | 0.6 ± 0.1 | 0.41 ± 0.04 | <0.05 | 0.7 ± 0.2 | >11.0 | 28 ± 9 |
| | Center | 462 ± 2 | 365.5 ± 0.4 | 23.6 ± 0.7 | 0.792 ± 0.003 | 19.5 ± 0.6 | 147 ± 1 |
| | Ring1 | 204 ± 1 | 155.4 ± 0.2 | 8.8 ± 0.6 | 0.762 ± 0.004 | 23.2 ± 1.5 | 137 ± 2 |
| | Ring2 | 115.0 ± 0.8 | 78.9 ± 0.2 | 4.2 ± 0.4 | 0.686 ± 0.005 | 27.4 ± 2.3 | 126 ± 2 |
| | Ring3 | 60.8 ± 0.8 | 38.5 ± 0.1 | 1.5 ± 0.2 | 0.633 ± 0.008 | 41.7 ± 7.0 | 112 ± 3 |
| | Ring4 | 33 ± 1 | 24.56 ± 0.1 | 1.1 ± 0.2 | 0.74 ± 0.03 | 29.5 ± 6.3 | 106 ± 13 |
| | Ring5 | 33.9 ± 0.9 | 19.33 ± 0.07 | <0.26 | 0.57 ± 0.01 | >128 | 105 ± 6 |
| | Ring6 | 27.9 ± 0.8 | 15.6 ± 0.1 | <0.26 | 0.56 ± 0.02 | >108 | 102 ± 7 |
| | Ring7 | 23.1 ± 0.9 | 12.83 ± 0.07 | <0.21 | 0.56 ± 0.02 | >107 | 91 ± 9 |
| | Ring8 | 17.0 ± 0.7 | 9.9 ± 0.1 | <0.19 | 0.58 ± 0.03 | >88.5 | 82 ± 8 |
| | Ring9 | 13.5 ± 0.7 | 8.23 ± 0.08 | <0.22 | 0.61 ± 0.03 | >60.9 | 82 ± 12 |
| NGC 3198 | Ring10 | 11.6 ± 0.5 | 7.15 ± 0.09 | <0.21 | 0.62 ± 0.03 | >56.0 | 87 ± 15 |
| | Ring11 | 11.2 ± 0.6 | 7.25 ± 0.09 | <0.25 | 0.65 ± 0.04 | >44.1 | 91 ± 18 |
| | Center | 8.0 ± 0.3 | 4.3 ± 0.1 | 0.8 ± 0.1 | 0.54 ± 0.03 | 10.0 ± 1.7 | 92 ± 7 |
| | Ring1 | 4.0 ± 0.3 | 1.98 ± 0.06 | <0.1 | 0.49 ± 0.04 | >41.9 | 63 ± 8 |
| | Ring2 | 1.9 ± 0.2 | 1.26 ± 0.04 | <0.05 | 0.68 ± 0.07 | >34.5 | 42 ± 9 |
| | Ring3 | 1.5 ± 0.2 | 0.64 ± 0.04 | <0.07 | 0.42 ± 0.07 | >21.5 | 33 ± 13 |
| NGC 3351 | Center | 17.5 ± 0.4 | 15.4 ± 0.1 | 1.3 ± 0.2 | 0.88 ± 0.02 | 13.5 ± 2.1 | 194 ± 8 |
| | Ring1 | 3.1 ± 0.4 | 1.8 ± 0.1 | <0.13 | 0.59 ± 0.08 | >23.2 | 96 ± 29 |
| | Ring2 | 3.6 ± 0.2 | 1.79 ± 0.06 | <0.13 | 0.50 ± 0.03 | >28.1 | 41 ± 5 |
| | Ring3 | 2.7 ± 0.3 | 1.08 ± 0.05 | <0.09 | 0.41 ± 0.05 | >29.8 | 40 ± 9 |

Table 5. (Continued)

| Galaxy | Region | $I_{12\text{CO}(1-0)}$ [K km s ⁻¹] (1) | $I_{12\text{CO}(2-1)}$ [K km s ⁻¹] (2) | $I_{13\text{CO}(1-0)}$ [K km s ⁻¹] (3) | $R_{2/1}$ (4) | $R_{12/13}$ (5) | ΔV [km s ⁻¹] (6) |
|----------|---------------------------|--|--|--|------------------|--------------------|--|
| NGC 3521 | Center | 32.3 ± 0.6 | 20.5 ± 0.2 | 2.8 ± 0.3 | 0.64 ± 0.01 | 11.7 ± 1.3 | 165 ± 13 |
| | Ring1 | 27.7 ± 0.4 | 17.8 ± 0.1 | 2.3 ± 0.1 | 0.64 ± 0.01 | 11.9 ± 0.8 | 118 ± 3 |
| | Ring2 | 16.8 ± 0.3 | 9.28 ± 0.08 | 1.0 ± 0.1 | 0.55 ± 0.01 | 17.1 ± 2.1 | 92 ± 3 |
| | Ring3 | 5.7 ± 0.3 | 3.15 ± 0.06 | 0.36 ± 0.07 | 0.55 ± 0.03 | 16.0 ± 3.2 | 88 ± 9 |
| | Ring4 | 2.1 ± 0.2 | 0.96 ± 0.05 | <0.09 | 0.46 ± 0.05 | >24.1 | 49 ± 9 |
| | Ring5 | 1.2 ± 0.1 | 0.59 ± 0.04 | <0.06 | 0.51 ± 0.07 | >19.3 | 56 ± 13 |
| NGC 3627 | Center | 50.4 ± 0.7 | 21.1 ± 0.6 | 2.0 ± 0.3 | 0.42 ± 0.01 | 25.3 ± 3.9 | 164 ± 9 |
| | bar | 24.7 ± 0.8 | 10.2 ± 0.2 | 1.2 ± 0.2 | 0.41 ± 0.01 | 20.3 ± 3.8 | 108 ± 11 |
| | Northern bar end | 31.9 ± 0.6 | 15.7 ± 0.2 | 2.8 ± 0.2 | 0.49 ± 0.01 | 11.5 ± 0.8 | 68 ± 3 |
| | Southern bar end | 41 ± 1 | 20.3 ± 0.2 | 3.3 ± 0.3 | 0.49 ± 0.01 | 12.5 ± 1.2 | 96 ± 11 |
| | Western arm | 13.7 ± 0.4 | 6.4 ± 0.1 | 0.9 ± 0.1 | 0.47 ± 0.02 | 15.1 ± 2.5 | 48 ± 2 |
| | Eastern arm | 18.4 ± 0.4 | 9.0 ± 0.2 | 1.7 ± 0.2 | 0.49 ± 0.02 | 11.0 ± 1.4 | 68 ± 3 |
| | Offset stream | 19.1 ± 0.5 | 9.7 ± 0.2 | 1.1 ± 0.2 | 0.51 ± 0.02 | 16.9 ± 3.2 | 60 ± 3 |
| | Southern arm | 11.1 ± 0.6 | 5.3 ± 0.1 | 0.7 ± 0.2 | 0.48 ± 0.03 | 15.0 ± 4.1 | 45 ± 3 |
| | Arm-bar end inter. region | 12.3 ± 0.4 | 4.4 ± 0.1 | <0.19 | 0.36 ± 0.02 | >65.4 | 51 ± 3 |
| | Inter-arm | 10.0 ± 0.5 | 4.7 ± 0.1 | <0.14 | 0.47 ± 0.03 | >70.5 | 86 ± 9 |
| | Outer disk | 2.6 ± 0.2 | 1.03 ± 0.07 | <0.09 | 0.39 ± 0.05 | >30.4 | 58 ± 12 |
| NGC 3938 | Center | 9.5 ± 0.2 | 5.98 ± 0.09 | 1.2 ± 0.1 | 0.63 ± 0.02 | 8.2 ± 0.8 | 43 ± 2 |
| | Ring1 | 6.4 ± 0.2 | 3.68 ± 0.05 | 0.63 ± 0.07 | 0.57 ± 0.02 | 10.1 ± 1.2 | 29 ± 1 |
| | Ring2 | 4.3 ± 0.1 | 2.46 ± 0.04 | 0.36 ± 0.05 | 0.57 ± 0.02 | 12.1 ± 1.9 | 28 ± 1 |
| | Ring3 | 2.4 ± 0.2 | 1.36 ± 0.04 | 0.35 ± 0.06 | 0.56 ± 0.05 | 6.9 ± 1.3 | 27 ± 3 |
| | Ring4 | 1.02 ± 0.09 | 0.55 ± 0.03 | <0.03 | 0.54 ± 0.06 | >29.7 | 24 ± 3 |
| NGC 4536 | Center | 34 ± 1 | 29.7 ± 0.2 | 2.0 ± 0.3 | 0.86 ± 0.02 | 17.0 ± 2.2 | 161 ± 17 |
| | Ring1 | 6.5 ± 0.4 | 4.9 ± 0.1 | <0.14 | 0.74 ± 0.05 | >45.1 | 136 ± 23 |
| | Ring2 | 2.2 ± 0.2 | 1.34 ± 0.07 | <0.1 | 0.61 ± 0.07 | >22.8 | 80 ± 16 |
| NGC 4579 | Center | 13.0 ± 0.7 | 10.1 ± 0.2 | <0.35 | 0.78 ± 0.05 | >37.0 | 154 ± 36 |
| | Ring1 | 5.5 ± 0.4 | 3.05 ± 0.09 | <0.2 | 0.55 ± 0.04 | >28.0 | 50 ± 6 |
| | Ring2 | 5.1 ± 0.2 | 2.68 ± 0.07 | 0.41 ± 0.08 | 0.52 ± 0.03 | 12.3 ± 2.5 | 50 ± 4 |
| | Ring3 | 2.8 ± 0.3 | 1.30 ± 0.08 | <0.13 | 0.47 ± 0.06 | >21.0 | 46 ± 11 |
| NGC 5055 | Center | 40.0 ± 0.6 | 27.3 ± 0.3 | 3.7 ± 0.3 | 0.68 ± 0.01 | 10.9 ± 0.8 | 120 ± 4 |
| | Ring1 | 20.1 ± 0.3 | 11.4 ± 0.1 | 2.4 ± 0.2 | 0.569 ± 0.01 | 8.4 ± 0.6 | 71 ± 2 |
| | Ring2 | 14.0 ± 0.2 | 6.79 ± 0.08 | 1.08 ± 0.09 | 0.484 ± 0.01 | 12.9 ± 1.0 | 53 ± 1 |
| | Ring3 | 8.5 ± 0.2 | 4.38 ± 0.07 | 0.82 ± 0.1 | 0.51 ± 0.02 | 10.4 ± 1.3 | 47 ± 2 |
| | Ring4 | 5.5 ± 0.2 | 2.74 ± 0.07 | 0.44 ± 0.07 | 0.5 ± 0.02 | 12.4 ± 2.1 | 44 ± 2 |
| | Ring5 | 2.7 ± 0.2 | 1.28 ± 0.05 | <0.06 | 0.48 ± 0.04 | >42.4 | 43 ± 4 |
| | Ring6 | 1.8 ± 0.2 | 0.65 ± 0.04 | <0.06 | 0.35 ± 0.04 | >30.5 | 49 ± 8 |
| | Ring7 | 1.1 ± 0.2 | 0.54 ± 0.06 | <0.06 | 0.51 ± 0.09 | >18.1 | 49 ± 12 |
| NGC 5713 | Center | 36.3 ± 0.7 | 34.4 ± 0.2 | 1.3 ± 0.2 | 0.95 ± 0.02 | 28.8 ± 5.7 | 112 ± 5 |
| | Ring1 | 20.7 ± 0.4 | 16.6 ± 0.1 | 0.8 ± 0.1 | 0.80 ± 0.02 | 24.5 ± 4.2 | 80 ± 4 |
| | Ring2 | 10.4 ± 0.4 | 7.1 ± 0.1 | <0.12 | 0.68 ± 0.03 | >86.2 | 61 ± 6 |
| | Ring3 | 5.7 ± 0.3 | 3.4 ± 0.1 | <0.11 | 0.59 ± 0.03 | >50.2 | 54 ± 5 |
| NGC 7331 | Center | 28.6 ± 0.9 | 17.6 ± 0.2 | 2.2 ± 0.3 | 0.61 ± 0.02 | 12.9 ± 1.6 | 143 ± 21 |
| | Ring1 | 35.2 ± 0.7 | 20.1 ± 0.1 | 4.3 ± 0.3 | 0.57 ± 0.01 | 8.1 ± 0.6 | 119 ± 9 |
| | Ring2 | 23.0 ± 0.4 | 12.8 ± 0.1 | 2.8 ± 0.3 | 0.56 ± 0.01 | 8.2 ± 0.8 | 114 ± 4 |
| | Ring3 | 11.6 ± 0.6 | 5.46 ± 0.1 | 1.0 ± 0.2 | 0.47 ± 0.02 | 12.0 ± 2.0 | 86 ± 10 |
| | Ring4 | 5.8 ± 0.4 | 2.60 ± 0.07 | <0.14 | 0.45 ± 0.04 | >40.6 | 93 ± 23 |
| | Ring5 | 3.1 ± 0.3 | 1.18 ± 0.07 | <0.11 | 0.38 ± 0.04 | >29.1 | 74 ± 20 |
| | Ring6 | 1.9 ± 0.2 | 0.66 ± 0.05 | <0.08 | 0.34 ± 0.05 | >23.5 | 67 ± 14 |

*(1) Integrated intensity of stacked ¹²CO(*J* = 1–0) spectra. (2) Same as (1) but for ¹²CO(*J* = 2–1). (3) Same as (1) but for ¹³CO(*J* = 1–0). (4) Integrated intensity ratio of stacked ¹²CO(*J* = 2–1) to ¹²CO(*J* = 1–0). (5) Same as (4) but for stacked ¹²CO(*J* = 1–0)/¹³CO(*J* = 1–0). (6) FWHM of stacked ¹²CO(*J* = 1–0) spectra.

References

- Bigiel, F., Leroy, A., Walter, F., Brinks, E., de Blok, W. J. G., Madore, B., & Thornley, M. D. 2008, *AJ*, 136, 2846
- Bolatto, A. D., Wolfire, M., & Leroy, A. K. 2013, *ARA&A*, 51, 207
- Braine, J., & Combes, F. 1992, *A&A*, 264, 433
- Casasola, V., et al. 2017, *A&A*, 605, A18
- Cormier, D., et al. 2018, *MNRAS*, 475, 3909
- Davis, T. A. 2014, *MNRAS*, 445, 2378
- Druard, C., et al. 2014, *A&A*, 567, A118
- Elmegreen, B. G. 2002, *ApJ*, 577, 206
- Gao, Y., Carilli, C. L., Solomon, P. M., & Vanden Bout, P. A. 2007, *ApJ*, 660, L93
- Gil de Paz, A., et al. 2007, *ApJS*, 173, 185
- Goldreich, P., & Kwan, J. 1974, *ApJ*, 189, 441
- Gong, M., Ostriker, E. C., Kim, C.-G., & Kim, J.-G. 2020, *ApJ*, 903, 142
- Heyer, M., Krawczyk, C., Duval, J., & Jackson, J. M. 2009, *ApJ*, 699, 1092
- Isobe, T., Feigelson, E. D., Akritas, M. G., & Babu, G. J. 1990, *ApJ*, 364, 104
- Israel, F. P., & Baas, F. 2003, *A&A*, 404, 495
- Kennicutt, R. C. 1989, *ApJ*, 344, 685
- Koda, J., et al. 2011, *ApJS*, 193, 19
- Koda, J., et al. 2012, *ApJ*, 761, 41
- Koda, J., et al. 2020, *ApJ*, 890, L10
- Komugi, S., Sofue, Y., & Egusa, F. 2006, *PASJ*, 58, 793
- Kroupa, P. 2001, *MNRAS*, 322, 231
- Krumholz, M. R., & McKee, C. F. 2005, *ApJ*, 630, 250
- Kuno, N., et al. 2007, *PASJ*, 59, 117 (K07)
- Leroy, A. K., et al. 2009, *AJ*, 137, 4670 (L09)
- Leroy, A. K., et al. 2013, *AJ*, 146, 19
- Leroy, A. K., et al. 2015, *ApJ*, 801, 25
- Leroy, A. K., Walter, F., Brinks, E., Bigiel, F., de Blok, W. J. G., Madore, B., & Thornley, M. D. 2008, *AJ*, 136, 2782
- Meier, D. S., & Turner, J. L. 2001, *ApJ*, 551, 687
- Meier, D. S., & Turner, J. L. 2004, *AJ*, 127, 2069
- Meier, D. S., Turner, J. L., & Hurt, R. L. 2000, *ApJ*, 531, 200
- Milam, S. N., Savage, C., Brewster, M. A., Ziurys, L. M., & Wyckoff, S. 2005, *ApJ*, 634, 1126
- Minamidani, T., et al. 2016, *Proc. SPIE*, 9914, 99141Z
- Momose, R., et al. 2013, *ApJ*, 772, L13
- Morokuma-Matsui, K., & Muraoka, K. 2017, *ApJ*, 837, 137
- Morokuma-Matsui, K., Sorai, K., Watanabe, Y., & Kuno, N. 2015, *PASJ*, 67, 2
- Muraoka, K., et al. 2016, *PASJ*, 68, 89
- Muraoka, K., et al. 2019, *PASJ*, 71, S15
- Nakai, N., Kuno, N., Handa, T., & Sofue, Y. 1994, *PASJ*, 46, 527
- Narayanan, D., Krumholz, M., Ostriker, E. C., & Hernquist, L. 2011, *MNRAS*, 418, 664
- Nishimura, A., et al. 2015, *ApJS*, 216, 18
- Oka, T., Hasegawa, T., Hayashi, M., Handa, T., & Sakamoto, S. 1998, *ApJ*, 493, 730
- Oka, T., Hasegawa, T., Sato, F., Tsuboi, M., Miyazaki, A., & Sugimoto, M. 2001, *ApJ*, 562, 348
- Onodera, S., et al. 2010, *ApJ*, 722, L127
- Paglionie, T. A. D., et al. 2001, *ApJS*, 135, 183
- Papadopoulos, P. P., van der Werf, P., Xilouris, E., Isaak, K. G., & Gao, Y. 2012, *ApJ*, 751, 10
- Peñaloza, C. H., Clark, P. C., Glover, S. C. O., & Klessen, R. S. 2018, *MNRAS*, 475, 1508
- Peñaloza, C. H., Clark, P. C., Glover, S. C. O., Shetty, R., & Klessen, R. S. 2017, *MNRAS*, 465, 2277
- Pineda, J. E., Caselli, P., & Goodman, A. A. 2008, *ApJ*, 679, 481
- Robitaille, T., & Bressert, E. 2012, *Astrophysics Source Code Library*, ascl:1208.017
- Sakamoto, S., Hasegawa, T., Handa, T., Hayashi, M., & Oka, T. 1997, *ApJ*, 486, 276
- Sakamoto, S., Hasegawa, T., Hayashi, M., Handa, T., & Oka, T. 1995, *ApJS*, 100, 125
- Sakamoto, S., Hayashi, M., Hasegawa, T., Handa, T., & Oka, T. 1994, *ApJ*, 425, 641
- Sandstrom, K. M., et al. 2013, *ApJ*, 777, 5
- Sawada, T., et al. 2001, *ApJS*, 136, 189
- Schmidt, M. 1959, *ApJ*, 129, 243
- Schruba, A., et al. 2011, *AJ*, 142, 37
- Schruba, A., Kruijssen, J. M. D., & Leroy, A. K. 2019, *ApJ*, 883, 2
- Scoville, N. Z., & Solomon, P. M. 1974, *ApJ*, 187, L67
- Sheth, K., et al. 2010, *PASP*, 122, 1397
- Sobolev, V. V. 1960, *Moving Envelopes of Stars* (Cambridge, MA: Harvard University Press)
- Solomon, P. M., Rivolo, A. R., Barrett, J., & Yahil, A. 1987, *ApJ*, 319, 730
- Sorai, K., et al. 2001, *ApJ*, 551, 794
- Sorai, K., et al. 2019, *PASJ*, 71, S14 (S19)
- Sun, J., et al. 2018, *ApJ*, 860, 172
- Sun, J., et al. 2020, *ApJ*, 901, L8
- Tan, J. C. 2010, *ApJ*, 710, L88
- Usero, A., et al. 2015, *AJ*, 150, 115
- van der Tak, F. F. S., Black, J. H., Schöier, F. L., Jansen, D. J., & van Dishoeck, E. F. 2007, *A&A*, 468, 627
- Walter, F., Brinks, E., de Blok, W. J. G., Bigiel, F., Kennicutt, R. C., Thornley, M. D., & Leroy, A. 2008, *AJ*, 136, 2563
- Yajima, Y., et al. 2019, *PASJ*, 71, S13
- Young, J. S., & Scoville, N. Z. 1991, *ARA&A*, 29, 581